Fachhochschule Flensburg

B A C H E L O R - T H E S I S

Thema: Combination of Shadow and Irradiance Data to Create Irradiance Maps

von: Thomas Haase

Matrikel-Nr.: 510315

Studiengang: Regenerative Energietechnik

Betreuer/in und Erstbewerter/in: Prof. Dr.-Ing. Volker Staben

Zweitbewerter/in: Prof. Dr. rer. nat. Tim Aschmoneit

Ausgabedatum: 14.01.2016

Abgabedatum: 14.03.2016

Selbstständigkeitserklärung

Ich versichere, dass ich die vorliegende Thesis ohne fremde Hilfe selbstständig verfasst und nur die angegebenen Quellen benutzt habe.

Datum: .....

(Unterschrift)

Table of Contents

Abstract

The exit from nuclear and fossil-fuel energy sources requires alternative energy sources to be tapped. Concentrating solar power (CSP) has proven to be an efficient source of renewable power. In order to operate solar power plants, it is necessary to understand its efficiency and energy yield in detail. If the direct normal irradiance (DNI) is only known for one or a few points in the solar field, errors can occur in the plant simulation and the plant control. The solar collectors, that provide the heat to the power block, cover approximately one square kilometer for 50 megawatt electrical turbine power. In this area, high variations of DNI can occur. For example, in parabolic trough fields four sub fields have their individual heat transfer fluid (HTF) flow control. Hence, the power plant control requires further information about inhomogeneous irradiance. In consideration of the fact, that the power plant operator wants to maximize the profit, he needs to know, how the power plant will perform within the next 0-15 minutes. Forecasting in this range is called "nowcasting". For nowcasting applications it is beneficial to create irradiance maps with cameras, that observe the sky, to document the current irradiance for every coordinate of the observed area, since the operator is able to preact to short term differences in the DNI, which lower the power plant's energy outcome.

There is a shadow camera system at Plataforma Solar de Almería (PSA), which is used to validate the nowcasting system. The system detects the cloud's shadows on the ground. It was extended from two to six cameras, that enable a 360° view around the installed tower power plant. Besides, the camera calibration was applied and older results were improved, so that an area of four square kilometers is evaluated. The cameras are recording series of two exposure times in 15 seconds intervals to ensure a high temporal resolution. There is also a sensor grid on the ground, measuring the global horizontal irradiance (GHI) and DNI. Its measured irradiance data was implemented to the shadow camera system. By using the shadow camera's sensor information, a relation between image information and incident irradiance was build. Therefore, it is possible to determine irradiance values for shaded regions, that are just defined by their image information.

Plain view images (orthogonal images) are created for the evaluated area. By analyzing three time stamps, it is possible to detect shadow information. The shadow's structure is described by applying global thresholds. Also, the pixel difference is build between a shadowless and the investigated time stamp. Ultimately, these differences are used to define a DNI difference and generate irradiance maps for the evaluated area.

Those resulting irradiance maps can be generated for each time stamp, if camera and irradiance data is given. It was possible to evaluate an entire day. The method's results are evaluated and its accuracy is discussed.

1 Introduction

The usage of solar energy is a crucial component of current and future energy systems. Concentrating solar technologies (CST) have proven to be a very efficient source of power. CST is distributed into concentrating solar power (CSP) and concentrating photovoltaics (CPV). Usual applications for CSP are parabolic troughs, solar towers or Fresnel collectors, which convert solar energy into heat and ultimately into power. The solar radiation, is partly originated by the angular region of the sky containing the sun, which builds the direct part of the composed radiation, and partly originated by the atmosphere, that reflects radiation to the ground coordinate, which builds the diffuse part of solar radiation. The DNI is very sensitive to atmospheric effects, such as aerosols (particles in the air) and clouds. Solar power plants require information about inhomogeneities in DNI to control the flow of HTF in the sub grids of their parabolic troughs. Therefore, a reliable determination of the incident irradiance is required, to operate a solar power plant properly. By creating maps of the incident irradiance, the power plant can be operated more efficiently, since its thermodynamic cycle and its parameters (flow rate of working fluid, controlling of mirrors) can be fine tuned. According to [27], a very short term forecast has been defined as 0 - 15min, which is therefore called "nowcasting".

Several nowcasting systems have been documented in the literature. For example, there is the system of the University of California in San Diego, which is described in [2]. Cameras with a 180° wide-angle objective (whole sky imagers (WSIs)) are used to determine the cloud coverage (CC) of the momentary cloud situation. By image processing, the cloud information is able to be gathered as a binary map. Also, the cloud's movement can be detected, while its shadow is projected to the ground. To evaluate the irradiance information a grid of six pyranometers is used. With this system, nowcasting for 5, 10 and 15min is enabled. At PSA, there is also a nowcasting system implemented, established by [18]. The system contains four WSIs, which are constantly observing the sky to detect clouds and project their shadow to the ground. Also, two shadow cameras were installed on top of the CESA-1 power tower to gather information about the actual shadow on the ground. Shadow cameras are observing the ground to create shadow maps. Those maps are used to validate the shadow map generated by WSIs. The shadow can be detected by creating orthogonal images of the ground. While there were no irradiance sensors implemented to the system, the area observed by shadow cameras was considerably low, since two cameras couldn't cover the area of PSA efficiently.

This thesis documents the enhancement of the existing shadow camera system at PSA. The existing system was extended, so that a wider area is covered by shadow camera generated image information. To generate ground information, all cameras need to be

calibrated, since this information is required to apply photogrammetrical functions, which ultimately create orthogonal images. Cleaning processes are applied afterwards. The segmentation needs to be improved as well, since the generated information was binary. Also the segmented pixel information shall be used, to gain information about the incident irradiance at the displayed coordinate. Therefore, a factor has been defined, that describes the relation between pixel difference and DNI difference. This relation can be applied afterwards to evaluate pixel information, that are not braced by sensor information to ultimately determine irradiance data from the appearing pixel difference. The entire process is distributed into hardware and software components. The hardware component is represented by image acquisition and irradiance measurements. Afterwards the processing with MATLAB (orthogonalization, segmentation, combination) represents the software component. Ultimately, the resulting irradiance maps for DNI and GHI are delivered. The entire process is shown in figure 1.

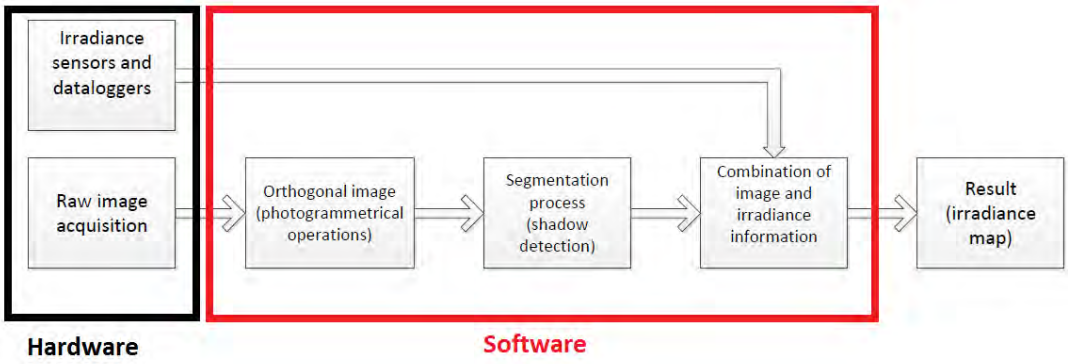

Figure 1: Flow chart of the entire process; distributed into hardware- and software components

In this thesis, the fundamentals for shadow camera systems and irradiance maps are explained in section 2 to understand an images composition and the irradiance component in a pixel value. Afterwards, the existing shadow camera system is analyzed in section 3.1, to understand, which changes have to be applied to the system, the orthogonal image and the following segmentation. Those final orthogonal images will be introduced in section 3.3. To gather shadow information, images from three time stamps have to be analyzed. This process is described in section 4. These resulting pixel differences will be used in section 5 to gain information about the observed area. Therefore, the relation between pixel difference and DNI difference is introduced in section 5.3 to determine irradiance values for shaded areas. The combined information of pixel differences and ground-based irradiance, measured by radiometers, leads to DNI and GHI maps, that are presented in section 5.5. Ultimately, the determined results are evaluated in section 6.

2 Fundamentals of Irradiance Maps

To create irradiance maps, which describe the irradiance at several locations in a field, it is required to understand irradiance and its composition, in order to understand the differences between shaded and sunny areas. Therefore, the irradiance composition and its source, the sun, are explained in the beginning of this chapter. Besides, atmospheric influences to the extraterrestrial irradiance are displayed and explained.
Moreover, the measurement devices are explained later on. Also, the camera's sensor is presented in detail. Consequently, it is also required to have a deeper understanding of the image composition and the influences, that determine a pixel's value in an image. Then, the photogrammetrical model will be introduced, since it is require to understand, how a camera is defined and which parameters are required to create orthogonal images. Ultimately, there will be a closer view to the shadow camera system, that has been used as the basis for further development in this thesis.

2.1 Electromagnetic Radiation and Reflection

2.1.1 Electromagnetic Radiation

For a deeper understanding of the introduced radiation, several physical quantities are required. These quantities are radiometric quantities as introduced in [29].

The radiant energy Q is determined as the sum of all incident photon's energies. If the radiant energy is observed during the unit of time $\mathrm{d}t$, the radiant flux Φ is determined.

$$\Phi = \frac{\mathrm{d}Q}{\mathrm{d}t} \tag{1}$$

The unity of Q is joule the unity of radiant flux Φ is watt. Power density E, respectively irradiance, is determined as the incident radiant flux to the unit area $\mathrm{d}A$. Hence, the irradiance is given by

$$E = \frac{\mathrm{d}\Phi}{\mathrm{d}A} \tag{2}$$

with the unity watt per square meter.

The incident irradiance E integrated over the unit of time $\mathrm{d}t$ defines the irradiation J in joule per square meter.

$$J = \int_{t_1}^{t_2} \mathrm{d}t \cdot E \tag{3}$$

There are also directed quantities, which are defined by determining the solid angle element Ω of its direction. Ultimately, the radiance L describes the radiant flux, received from unit area $\mathrm{d}A$, emitted towards solid angle element $\mathrm{d}\Omega$. L is displayed in equation 4

$$L = \frac{\mathrm{d}^2\Phi}{\mathrm{d}A_\perp \mathrm{d}\Omega} \tag{4}$$

with the unity watts per square meter and steradian. With these quantities, it is possible to describe the appearing reflection in a certain area.

2.1.2 Reflection

If radiation is confronted with the border area between two media, it either gets transmitted, absorbed of reflected [9]. Following the law of energy conversation, these three fractions add up to one. The reflected part of radiation can be described by the bidirectional reflectance distribution function (BRDF) of the reflecting object. The reflected radiance L_r is received for the incident radiation of irradiance E_i. This relation is displayed in equation 5.

$$BRDF(\theta_\mathrm{i}, \varphi_\mathrm{i}, \theta_\mathrm{r}, \varphi_\mathrm{r}) = \frac{L(\theta_\mathrm{r}, \varphi_\mathrm{r}, E_\mathrm{i})}{E(\theta_\mathrm{i}, \varphi_\mathrm{i})} \tag{5}$$

The incident radiation's direction is defined by azimuth angle φ and elevation angle θ, while the observer's direction is defined by φ_r and θ_r as seen in figure 2 (left). The $BRDF$ is a material property, that does not change, if the reflectance remains constant as described in [16].

To describe reflection, two limit cases are defined. Those cases are specular reflection and diffuse reflection as seen in figure 2.

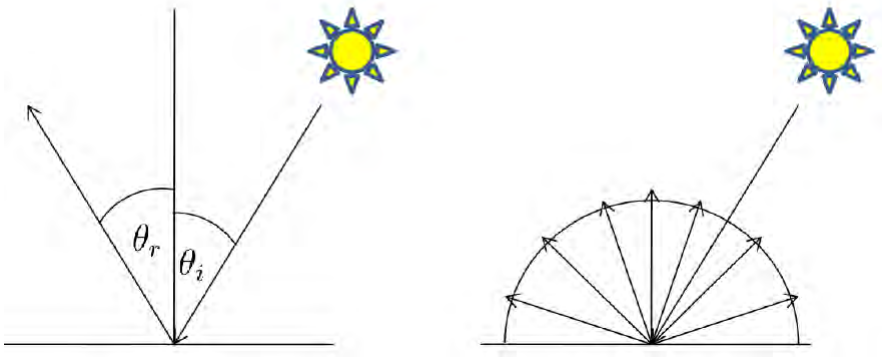

Figure 2: Mirror reflection (left) and diffuse reflection (right) from [19]

In case of specular reflection, the law of reflection applies, which defines $\theta_r = \theta_i$. The azimuth angle is consequently determined as $\varphi_r = \varphi_i + \pi$. Specular reflection is caused by the object's surface properties. If its irregularities are small, compared to the incident light's wavelength, it is reflected. Therefore, polished objects appear to reflect the incident light, since its surfaces irregularities are compensated.

An object reflects diffuse, if its surface is rough, compared to the light's wavelength. Then, the incident light is reflected homogeneously into all directions.

2.2 Solar Radiation and Attenuation in the Atmosphere

The sun works as a fusion reactor that converts four million tonnes of hydrogen into helium per second. Its surface temperature is approximately 5780 Kelvin as mentioned in [1] and radiates energy to the space. Since the earth moves around the sun and its path does not describe a perfect circle but an ellipse, the extraterrestrial irradiance differs during the year. As described in [11], the irradiance differs from 1415 watts per square meter at perigee (around the third of January) to 1321 watts per square meter at apogee (around the fourth of July). This results in an average total solar irradiance (TSI) of approximately 1361 $\pm$ 7 watts per square meter [6]. It is also recorded as solar constant, while its value and uncertainty is mentioned differently. The measured value of irradiance at the ground depends on extinction processes in the atmosphere and the sun's position, respectively the optical path it has to take. The path is described by the air mass. To describe the behavior of extinction and the effect of an alternating sun position, a definition of the sun's position is necessary. In figure 3 the angles θ_{el},θ_Z and θ_A are shown. θ_{el} is the elevation angle. It is measured up from horizon and defines the height of the sun. θ_A is the azimuth angle, which describes the sun's deviation from the northern axis. Thus, it is measured from north. Besides, there is θ_Z which is the zenith angle. It displays the deviation from zenith axis and is also defined by equation 6.

$$\theta_Z = 90^\circ - \theta_{el} \tag{6}$$

In the further observation it is determined with the Michalsky algorithm, which is documented in [17].

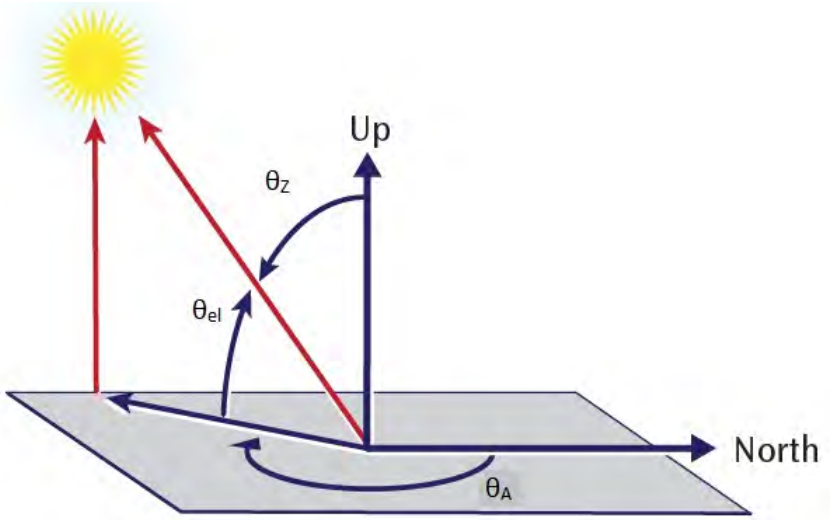

Figure 3: Angular variables to describe the suns position from [22]

2.2.1 Attenuation of Solar Radiation in the Atmosphere

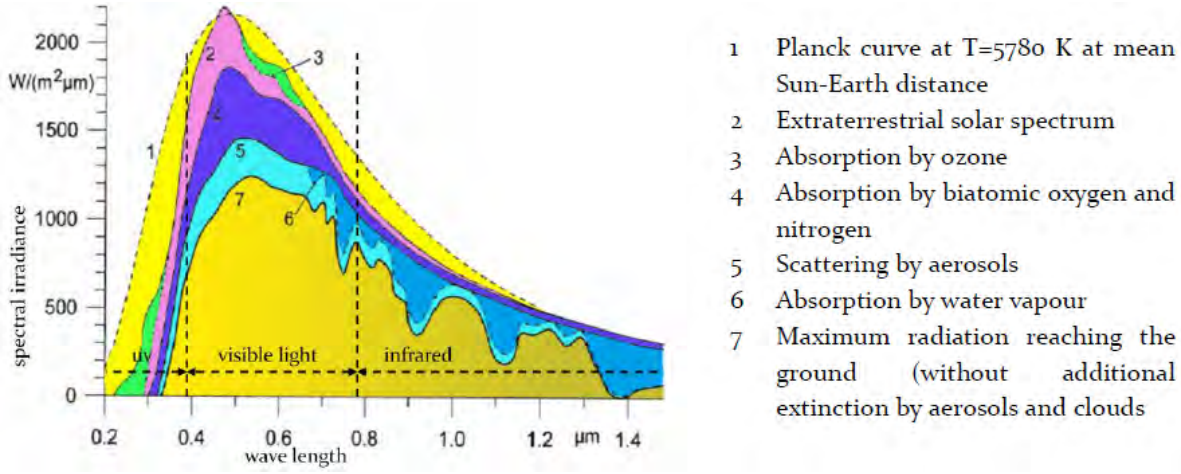

Figure 4: Reduction of DNI through atmospheric extinction processes from [8]

The solar beam is reduced by atmospheric extinction processes as it travels through the atmosphere. Extinction is the sum of absorption and scattering effects as displayed in figure 4.

1. Absorption
   The atmosphere contains molecules, that can absorb energy from photons [12]. Due to the energy transfer the molecule starts to vibrate. The absorption of photons depends on the complexity of the molecule. There is also a wavelength dependency in the absorption process. While N_2, O_2 and O_3 are the major contributors to absorption in the ultraviolet wavelength range, H_2O-vapour and CO_2 are the sources of absorption in the near infrared.

2. Scattering

   When a solar beam is colliding with dust particles or molecules, it is deviated from its original direction. This process is called scattering. Since the radiation can be scattered, diffuse horizontal irradiance (DHI) exists. Scattering is dependent on particle size and shape. It mainly occurs as Rayleigh - and Mie-scattering in the atmosphere:

   a) **Rayleigh-scattering** describes the reaction of electromagnetic radiation to particles, that are smaller than the wavelength of the radiation. As mentioned in [8], Rayleigh-scattering cross section follows approximately the wavelength to the power of minus four - law. Because of this, smaller wavelengths are scattered more than longer wavelengths. This also explains the changing in appearance of the sky during the day. While the sun is close to the zenith, the sky appears blue, because its short wavelength is scattered less. When the sun rises or sets, the light is scattered differently. A big fraction of short wavelengths is scattered off. This happens, since the light passes a longer distance compared to close-to zenith circumstances. Then, a higher fraction of long wavelengths is part of the radiation and the sky appears reddish.

   b) **Mie-scattering** is caused by particles, that have approximately the same size as the wavelength of the radiation. In opposite to Rayleigh-scattering it has a less pronounced dependency on wavelength. Bigger particles such as clouds, ice crystals, aerosol particles or water droplets cause Mie-scattering.

2.2.2 Air Mass

While the radiation is affected by particles in the atmosphere, there is also a dependency on geographical location and time. When the irradiance travels through the atmosphere, its attenuation grows with the distance. During sunset or sunrise for instance, the irradiance measured on the ground is significantly reduced. That said, the highest DNI is measured during zenith hours. [8] approximates this interconnection in dependence on the solar zenith angle (SZA) θ_Z in equation 7.

$$AM = \frac{1}{\cos \theta_Z} \tag{7}$$

This relation is illustrated in figure 5.

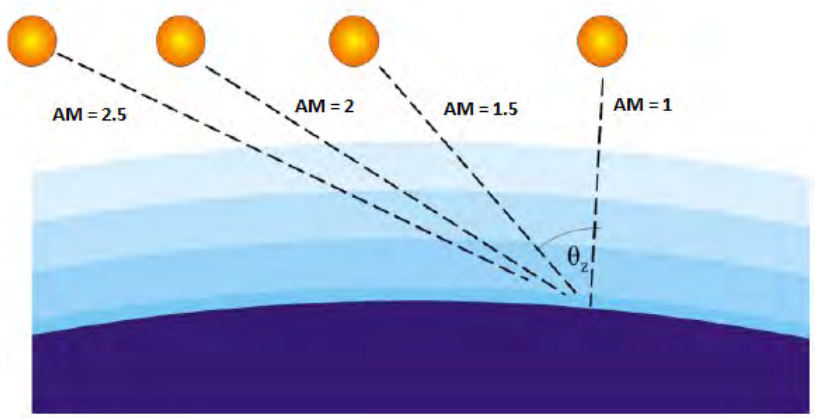

Figure 5: Air mass with different SZA from [8]

2.2.3 Components of Solar Irradiance

[11] describes, that there are three fundamental components of the solar radiation, reaching the earth's surface:

1. **Direct horizontal irradiance (DNI)** is solar beam radiation, which is directly emitted from the sun's disk to a given surface on the ground, which is orthogonal to the solar beam. It is measured by pyrheliometers that are introduced in 2.3.

2. **Diffuse horizontal irradiance (DHI)** includes all incoming radiation excluding DNI. The remaining part describes all scattered irradiance, measured on a horizontal surface. Objects like clouds, buildings, atmospheric constituents like aerosols or even animals and bushes can increase the amount of DHI.

3. **Global horizontal irradiance (GHI)** includes all incoming irradiance on a horizontal surface. Including both: DHI and DNI. Since the DNI differs throughout the day, its component in GHI also differs. The three components are connected by equation 8.

$$GHI = DHI + DNI \times \cos(\theta_Z) \tag{8}$$

2.3 Irradiance Measurement

Meteorological radiation instruments determine the amount of solar irradiance by measuring a current, caused by solar irradiance. The specification of instruments for the measurement is established by [26]. Besides, it is defined that hemispherical solar and direct solar radiation is integrated over the spectral range of 0.3 μm to 3 μm. How well a sensor can display the incident radiation is also described by its spectral response. A photoelectric sensor's spectral response for example is worse than the thermopile's since there are photons, that are too weak to loosen an electron to create a photo current. Thus,

the energy of this photon is not displayed in the resulting current. On the other hand, there are photons of shorter wavelengths, which contain more energy but still only one electron is emitted. Therefore, thermopiles usually have better spectral responses than photoelectric sensors.

2.3.1 Pyranometer

To measure the GHI pyranometers are used. Field pyranometers also use blackened thermopiles as sensor elements to determine voltage signals. There are also photoelectric pyranometers that use photodiodes instead of thermopiles. Field pyranometers are usually placed under two glass domes. But diffusor disks are also used for this purpose as mentioned in [28]. The pyranometers used for this work are silicon based semi conductors. While they are actually not considered pyranometers according to [7] and [26], they were cost efficient and less maintenance intense [30]. It was possible to build a grid of twenty pyranometers to evaluate the irradiance in a certain area on the PSA. Pyranometers are also used to gain information about the DHI. The PSA high precision (HP) station is shown in figure 6. A shading device is used to exclude DNI. This application uses a shadow ball (see figure 6b, red box) to shadow the sensor but shading discs can also be used. Since the shading device needs to exclude the sun, it is required to be tracked as well.

(a) Pyranometer (b) Shading device

Figure 6: Image of field pyranometers installed to the PSA HP station. The field pyranometer is shown in 6a while its shading device is displayed in 6b

2.3.2 Pyrheliometer

Pyrheliometers are used to measure the DNI. Their sensor element is placed behind an aperture and a collimator tube, which enables the radiation to reach the sensor. The aperture and the collimator allow only a small angular region of the incidental light reaches the sensor. The aperture is protected by a small window to exclude exterior influences like rain or dust to reach the sensor. They usually use blackened thermopile sensors, since

these are enabling a flat spectral response covering nearly the complete solar spectrum. The voltage of the thermopile is proportional to the incident irradiance as mentioned in [28]. To compute a DNI signal out of the measured voltage signal, their calibration factor is needed. There are also pyrheliometers with photoelectric sensors, but they do not provide the spectral range to be called pyrheliometer following [7].
To maintain that the sensor's surface is directed orthogonally to the incident irradiance, the pyrheliometer is mounted on a tracker, which is shown in figure 7.

Figure 7: Image of two field pyrheliometers installed to the PSA HP station; mounted on a tracker to measure DNI depending on sun's position.

To determine the GHI, the most accurate way is to derive it from measurements of DNI and DHI. They are measured more accurately, since good quality pyrheliometers have lower uncertainties than the most accurate pyranometers as seen in [28] and [7]. Ideally, the measured GHI is only used to verify the calculated GHI.

2.4 Image Recording

2.4.1 Camera Sensor

For the detection of the light's information a complementary metal oxide semiconductor (CMOS) is used. It converts the incident light to an electric charge and ultimately into a digital signal by using transistors, which are arranged in a matrix. In contrast to charge coupled device (CCD) sensors, which are the alternative to CMOS sensors, every image pixel contains its own capacitor in combination with an output amplifier as mentioned in [3]. CMOS sensors generate a digital output, since the signal processing is partly is accomplished within the chip. The general structure of a CMOS sensor is displayed in figure 8.

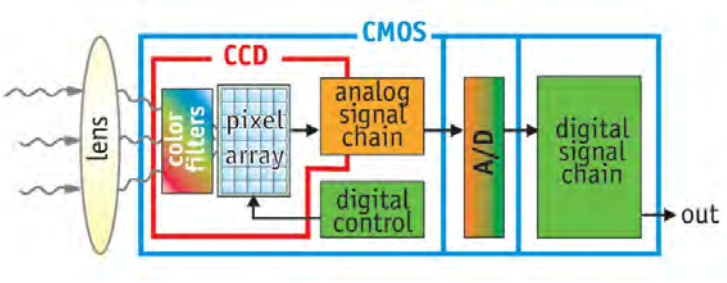

Figure 8: Functionality of a CMOS sensor from [13]

To gain information about the incident light, there are color filters between lens and the mentioned pixels. Those are colored red, green and blue, which is causing a current in the corresponding pixel. They are usually arranged in a Bayer pattern. This means, that there are 50 percent of the matrix are covered by green filters, while each of the red and blue channel covers 25 percent of the matrix.

The final parameter to be introduced is the sensor's spectral response. The spectral response however, is defined by the diode's quantum efficiency. The quantum efficiency $QE(\lambda)$ defines the relation between the amount of build electron-hole pairs, caused by the inner photo effect, and the amount of quantum of wavelength λ, as seen in [29]. To create a connection to the spectral irradiance E_λ, the spectral response $\varepsilon(\lambda)$ is defined. e displays the elementary charge. With $c_\lambda = \lambda \cdot f$ equation 9 applies.

$$\varepsilon(\lambda) = \frac{QE(\lambda) \cdot \lambda}{h \cdot c_\lambda} \cdot e \tag{9}$$

2.4.2 Composition of Image Information

The normalized pixel vector $\vec{S'}_{\text{sensor}}$, derived from the sensor, is multiplicated with the camera specific 3×3 matrix M_{cam} into the value of the preliminary color channels Red Green Blue (RGB). M_{cam} is applied and defines S'_{M}, since the spectral response between the human eye and a photo diode [21] differ, the image does not display white values, that are familiar with the human sense of white values. An exemplary M_{cam} is shown in [21]:

$$M_{\text{cam}} = \begin{bmatrix} 0.618637 & 0.252417 & 0.113803 \\ 0.367501 & 0.579499 & 0.052999 \\ 0.000466 & 0.005067 & 0.749913 \end{bmatrix} \tag{10}$$

M_{cam} is a camera specific value. Afterwards, $\vec{S'}_{\text{M}}$ is transformed to standard Red Green Blue (sRGB) values by applying the gamma correction Γ_{sRGB}. Those have to be transformed, since the physical sensor signal is linear related to the irradiation on a pixel.

Hence, the RGB values are transformed by a non linear transfer function. The function is mentioned in [21] and displayed in equation 11.

$$S = \begin{cases} 12,92S'_{\mathrm{M}} & ,if \quad 0 \leq S'_{\mathrm{M}} \leq 0.03928 \\ 1.055S'^{\frac{1}{2.4}}_{\mathrm{M}} - 0.055 & ,if \quad 0.03928 \leq S'_{\mathrm{M}} \leq 1 \end{cases} \tag{11}$$

The normalized values are multiplicated by their colorspace factor, to obtain the pixel value in a JPEG image. For sRGB values this factor is 255 [10]. The digital image S_{255} is therefore build by

$$S_{\mathrm{sRGB}} = S \cdot q_{\mathrm{sRGB}} \tag{12}$$

Special cameras are able to take images, that are not affected by any gamma functions. Since the used cameras are usual security cameras, this transformation has to be negated. By doing so, the displayed value in an image gives more accurate information about the spectral irradiance falling onto sensor coordinate m, n. The linearization is applied in section 5.1.

Consequently, the value of a pixel in one color channel S_{sRGB} is defined by [29] as

$$S_{\mathrm{sRGB}} = \Gamma_{\mathrm{sRGB}}(M_{\mathrm{cam}} \int_{Amn} \mathrm{d}A \int_{\lambda_{\min}}^{\lambda_{\max}} \mathrm{d}\lambda \cdot t_{\mathrm{exp}} \cdot \vec{\varepsilon_{\mathrm{N}}} \cdot E_{\lambda}) + MasterPed \tag{13}$$

- Γ_{sRGB} = Function, that converts image values, that are linear to the sensor signal, into corresponding sRGB (see equation 11)
- M_{cam} = 3×3 matrix, that applies white balance and transformation of color system (see equation 10)
- A_{mn} = Area at one pixel
- λ = Wavelength : $\lambda_{\min}$ and $\lambda_{\max}$ define the spectral range
- t_{exp} = Exposure time
- $\vec{\varepsilon_{\mathrm{N}}}$ = Camera's normalized spectral response. This displays the CMOS spectral response in terms of linear pixel values S'_{sRGB} Its unity is joule times meter to the power of minus one.
- E_{λ} = Spectral irradiance
- $MasterPed$ = Offset for every color channel. If the camera takes an image in total darkness, the $MasterPed$ is found in the image.

2.5 Photogrammetrical Model

To derive the shadow information, the raw images have to be displayed in a plain view, which is realized by creating orthogonal images. Orthogonal images display the area observed, while compensating the distortion, caused by the tilted perspective of introduced cameras. To accomplish this, camera constant, interior and exterior orientation and distortion parameter need to be characterized and defined. The model of the pinhole camera is a common methodology to describe cameras. The camera displays object points by using the physical model of the central projection. [14] describes a lensless camera, that displays the incident cone of rays, intercepting in the projection center O, onto the sensor without distorting them. In reality, the cone of rays is distorted by the lenses inside the camera. Goal of every photogrammetrical observation is to describe the displaying properties between the existing object point P and the corresponding image point P'. This is described by different transformations (rotation, translation, scaling) in different coordinate systems as mentioned in [18].

Cameras with lenses are displaying a distortion between object point and image point, due to the fact, that the light is concentrated in the lens and projected onto the sensor. This difference is characterized by the radial symmetrical distortion $\Delta r'$. Therefore, real cameras differ from the model of central projection. Consequently, a different camera model needs to be applied. Mentioned model is determined by displayed in figure 9

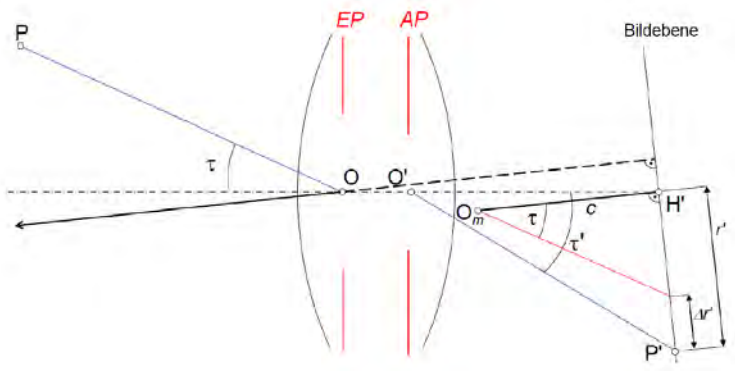

Figure 9: Sketch of modified camera model. Image from [18]

Most camera models are referring to the projection center O', which represents the lenses center of exit (AP, *Austrittspupille*), seen from the images side of the camera system. Its position in the global system is defined by the exterior orientation parameters. Figure 9 displays a sketch for a camera with several lenses. Beside the radial symmetric distortion, the tilted optical axis $O_{\mathrm{m}}H'$, which causes a further distortion, is displayed. This describes the principal points (H') deviation from the actual image center. Mentioned deviation is also determined during the calibration of the interior orientation.

2.5.1 Coordinate Systems and Displaying Functions

For the definition of the camera's position and the application of mentioned transformations (rotation, translation, scaling), from the three dimensional object coordinates to two dimensional image coordinates, appropriate coordinate systems have to be defined. The following coordinate systems are defined by following [14].

- **Object coordinate system** describes the global coordinate system. Every object P, as well as the projection center O' are defined by its global positioning system (GPS) coordinates. The origin for this work is located east from the CESA-1 tower at (37.0939 °N; -2.359 °E; 504.25 meters above mean sea level (m.a.m.s.l.)).
- **Camera coordinate system** is a local coordinate system linked to the camera position (X^*, Y^*, Z^*). The origin of this system is located in the projection center O' of the corresponding camera. Image coordinates (x', y') can be defined in this system. Ultimately, the parameters required for the translation between this system and the object coordinate system are given by the exterior orientation.
- **Sensor coordinate system** can be used to describe the position of the image coordinate P' in the sensor plane. This system is two dimensional and limited by the width and length of the sensor. The camera constant c, as seen in figure 10 describes the distance between sensor area and the projection center O'.

The introduced coordinate systems are displayed in figure 10.

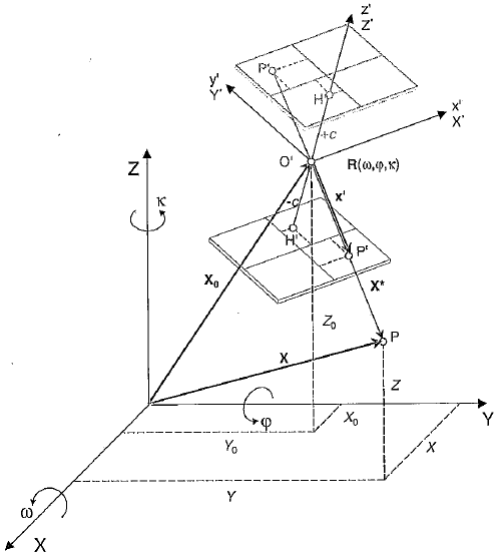

Figure 10: Sketch of central projection. Displaying global and local coordinate systems for photogrammetrical applications from [14]

For the central projection the collinearity equations apply to describe the relation between global coordinate X and Y and image coordinate x' and y' under the condition, that all eleven calibration parameters are determined. These include six exterior parameters $(X_0, Y_0, Z_0, \kappa, \omega, \varphi)$ and five interior parameters $(x'_0, y'_0, c, \Delta x', \Delta y')$. For the actual definition of the collinearity equations, the rotation matrix R has to be introduced first. It describes the rotation, that has to be applied to the object coordinate system for the transformation of local camera system's values. [14] describes R as

$$R = \begin{bmatrix} r_{11} & r_{12} & r_{13} \\ r_{21} & r_{22} & r_{23} \\ r_{31} & r_{32} & r_{33} \end{bmatrix} \tag{14}$$

The matrix elements are determined by the exterior parameters κ, ω and φ. Determined by a defined order the rotation is applied, all matrix elements are determined as

$$R = \begin{bmatrix} \cos\varphi\cos\kappa & -\cos\varphi\sin\kappa & sin\varphi \\ \cos\omega\sin\kappa + \sin\omega\sin\varphi\cos\kappa & \cos\omega\cos\kappa - sin\omega\sin\varphi\sin\kappa & -\sin\omega\cos\varphi \\ \sin\omega\sin\kappa - \cos\omega\sin\varphi\cos\kappa & \sin\omega\cos\kappa + \cos\omega\sin\varphi\sin\kappa & \cos\omega\cos\varphi \end{bmatrix} \tag{15}$$

With this information about the rotation matrix parameters, the collinearity equations are given as

$$x' = x'_0 - c \cdot \frac{r_{12} \cdot (X - X_0) + r_{21} \cdot (Y - Y_0) + r_{31} \cdot (Z - Z_0)}{r_{13} \cdot (X - X_0) + r_{23} \cdot (Y - Y_0) + r_{33} \cdot (Z - Z_0)} + \Delta x' \tag{16}$$

$$y' = y'_0 - c \cdot \frac{r_{12} \cdot (X - X_0) + r_{22} \cdot (Y - Y_0) + r_{32} \cdot (Z - Z_0)}{r_{13} \cdot (X - X_0) + r_{23} \cdot (Y - Y_0) + r_{33} \cdot (Z - Z_0)} + \Delta y' \tag{17}$$

2.5.2 Interior Orientation

The interior orientation describes the deviation of the light's path in the camera from the mathematical model of central projection. The connection between the projection center O' and the image area is called image vector $\vec{x'}$. Therefore, its distortion parameters have to be defined. Also the deviation of principle point H' to the image center is going to be defined. Consequently, the parameters to be determined are:

- Principle point $H' = (x'_0, y'_0)$ describes the dropped perpendicular foot of the projection center onto the image area
- Camera constant c describes the distance between projection center and the principle

point.

- Distortion parameters $\Delta x', \Delta y'$, which describe the deviation from the mathematical ideal construct of central projection. $\Delta r'$ describes the imaging error in both directions ($\Delta x'$,$\Delta y'$)

The imaging error is composed out of multiple effects like distortion, affinity and shear [14]. However, the radial symmetric distortion displays the main part of the resulting imaging error. The introduced polynomial describes the imaging error between an object coordinate and the corresponding image coordinate. There are multiple models to describe this polynomial. Its accuracy depends on the image radius. Luhmann's description of the polynomial displays weaknesses for wide-angle cameras. Therefore, the model introduced by [24] is used. [24] created a camera model for omnidirectional respectively fisheye cameras. These could potentially display the images for all directions, even behind the camera, which is realized by mirrors and lenses. For this purpose, the system is still considered appropriate, which is based on the general definition of the distortion function. The distortion function F is defined generally as a Taylor polynomial and displayed in equation 18.

$$\begin{aligned} F(m,n) &= a_0 + a_2 \cdot \rho'^2 + ... + a_N \cdot \rho'^N \\ mit \qquad \rho' &= \sqrt{m^2+n^2} \qquad und \qquad \frac{dF}{d\rho'} = 0 \end{aligned} \tag{18}$$

The definition of the camera's interior parameters is explained in section 3.2.2.

2.5.3 Exterior Orientation

The definition of exterior orientation parameter describes the camera's position and angular orientation in the object coordinate system. The orientation is defined by three translation parameters (X_0, Y_0 and Z_0), which define the camera's projection center O' in the object coordinate system, as well as three rotation parameters (ω, κ and φ). The rotation parameters describe the tilt of the camera's optical axis to the object coordinate system. The initial values for O' are given by GPS coordinates. In the context of given GPS information, the camera's position can be determined down to a deviation from its actual position of a few meters. The determination of the rotation parameters is realized by a numeric method, which uses the collinearity equations 16 and 17. To determine the rotation parameters, objects in the displayed area (x',y') and their coordinates (X, Y and Z) need to be defined. Under the circumstances of the previously determined interior

orientation parameters, the rotational parameters can be approximated. The detection of the camera's exterior orientation is explained in section 2.5.3.

2.6 State of the Art of Shadow Cameras

On the area of the PSA, there is a shadow camera system installed to detect cloud's shadow on the ground. This system is based on the work of [5], which was enhanced and presented in [25]. By using multiple cameras respectively their generated data, it is possible to determine shadow's position. In addition, four WSIs are installed for the detection of clouds. They convert binary images, containing the cloud's position in the image, to three dimensional coordinate of the clouds [20]. The model's shadow is projected to the ground by defining the sun's position. To validate the WSI based shadow information, shadow cameras serve as a validation system. For the validation, two cameras were already installed before this thesis. They are placed on the CESA-1, to gain shadow information from the ground. Both cameras are installed in a height which was estimated by [18] and mentioned as 85 meter above ground level (585 m.a.m.s.l.).

2.6.1 Shadow Cameras

For image recording, two M24M security cameras, produced by the MOBOTIX company, are used to gather shadow information of the observed area. Therefore, the cameras are referred to as shadow cameras. These cameras are producing reliable image information, while displaying low acquisition costs. They are dust- and water-jet-proof, according to [15]. The integrated CMOS sensor is enabling images with a 3.1 megapixel resolution (QXGA standard with 2048×1536 pixels). The camera specifications are summarized in table 1.

Camera data			
Model:	MX-M24M-Sec-D22	Lens:	L22
Dimensions / mm :	140.5 × 189 × 222	Focal length / mm :	22
Weight / g :	450	Sensor :	CMOS, 3.1 MP
Operating conditions:	IP66; -30 to +50 °C	Resolution / pixels :	2048×1536

Table 1: Camera and objective / sensor data for Mobotix M24M

Figure 11: Installed Mobotix M24M security camera (left) with the corresponding image (right)

All cameras are controlled by a controlling PC, which sets their exposure times and timers. To evaluate ground information, exposure times of 1280 μs are used, since shadow information can be gathered well due to the contrast. All image processes, that are required e.g. automatic contrast or effects of chroma, are applied afterwards. This ensures homogeneous data, whose properties can be adjusted program internally. Hence, the shadow camera's images are as raw as possible except of the mentioned linearization (see section 2.4.2).

2.6.2 Orthogonal Images

The documented shadow information is projected to the ground, by using the projection equations from section 2.5. Hence, the cameras were calibrated by using [23] for the interior orientation and a numeric optimization, which optimized three of six exterior orientation parameters (ω, κ and φ), while the position was defined by handheld GPS devices. Therefore, orthogonalized images of the documented area resulted. To project the raw image onto the field of the PSA, pixel coordinates have to be assigned to global coordinates as mentioned in 2.5.2. There are pixels, that are georeferenced by their features (in particular, the object in the pixel can be identified in Google Earth or directly from the ground). Hence, it's possible to create a georeferenced image in which global coordinates are assigned to each pixel. To orthogonalize the raw images entirely, the surface of the PSA is approximated by a polygonal chain, which is build by interpolating bilinearily between the existing features' GPS coordinates in the object coordinate system. The resulting polygonal area is rastered with a resolution of 1 square meter per pixel, which ultimately defines the image's grid size. Afterwards, the pixel coordinates are projected onto this model, which describes the area's differences in height. The assignment of pixel information to GPS coordinates is documented in a lookup table. Since parts of the

area are covered by both cameras, there is an overlapping area. This area is defined by interpolating each of the three color channels from both cameras information bilinearly, which results in a blurred image area, if both images don't coincide perfectly. Merged images covered an area of 781 · 1369 square meters. The process with its settings is displayed in figure 12.

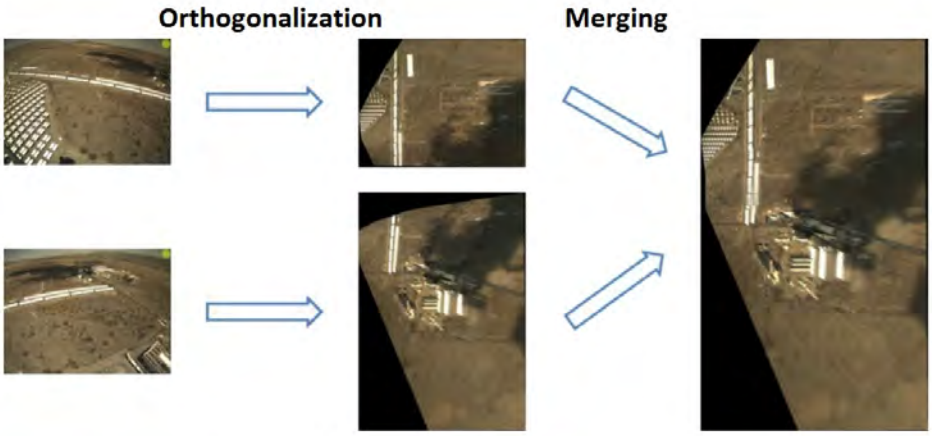

Figure 12: Process of orthogonal image creation with old boundary conditions from [18]

2.6.3 Segmentation

To segment the actual shadow information from the image, two time stamps were compared. By defining time stamps that display shadowless conditions, it is possible to segment the shadow from the time stamp, which was segmented by subtracting the evaluated time stamp from the shadowless time stamp. These reference time stamps are called shadowless events. In those the WSIs display shadowless conditions in their images or clouds, that do not shade the observed area. For the detection of clouds within an image the value CC was implemented. [18] specified the percentage cloud coverage as

$$CC = \frac{\sum_{i=1}^{N} P_{\text{cloud},i}}{N} \cdot 100 \tag{19}$$

With $P_{\text{cloud},i}$ defined, if it is a cloud. Then it contains the logical value "1" and "0" if it isn't a cloud. N is the total evaluated amount of pixels in the image. If the CC of all WSI approve, that the CC value is less than 1 percent, the time stamp is detected as a shadowless event. Also, if the detected clouds display an angular distance greater than 45° from solar position, the time stamp is also detected as a shadowless event since their shadows do not affect the area of PSA.

For the segmentation of image information, the basic pixel difference defined by [18]

is displayed in equation 20. $S_{\text{diff},mn}$ is build between the grayscale images of the non linearized orthogonal image for the shadowless time stamp $S_{\text{shadowless},mn}$ and the evaluated time stamp $S_{\text{eval},mn}$.

$$S_{\text{diff},mn} = S_{\text{shadowless},mn} - S_{\text{eval},mn} \tag{20}$$

Then, the application of the global threshold $T_{\text{g,ortho}}$ led to the resulting difference values. The result was a binary map, that contained information about the form and position of the cloud's shadow. Shadow information is defined, when the criteria

$$S_{\text{diff}mn} > T_{\text{g,ortho}} \tag{21}$$

is fulfilled. The segmentation result for these settings is displayed in figure 13.

Figure 13: Process of orthogonal image creation with old boundary conditions from [18]

3 Creation of Enhanced Orthogonal Images

In this section, the expansion of the existing shadow camera system is documented. Afterwards, the camera calibration is applied. Also processes, that are established to improve the orthogonal image's quality, are described. To gather shadow information from the ground, the existing shadow camera structure, established by [18] and displayed in section 2.6 at PSA, is used. While using them, it is possible to create orthogonal images and segment shadow information from those. The system is improved and enhanced by crucial components, such as the installation of four new cameras, to evaluate the entire PSA in the framework of the thesis. To determine, which components had to be improved, the previously existing system, introduced in section 2.6, was analyzed in section 3.2.1. This way, it is possible to determine which components have to be added respectively improved, to create orthogonal images, that deliver clear information about a shadow's position, structure and ultimately enable good segmentation results in the further processing. Afterwards, in section 3.2 the camera parameters are determined, since all cameras need to be recalibrated. The determination of those parameters enables dewarped, so called "orthogonal" images. By also executing exclusion processes to the resulting images, it is possible to create new orthogonal images, that display every coordinate of PSA (section 3.3). These orthogonal images are the basis of segmentation in section 4 and referred to as S_{sRGB}.

3.1 Analysis of the two Camera System

For the purpose of determining shadow information, the previously existing validation system has been enhanced. That was required, since it displayed some weaknesses in the creation of orthogonal images.

The system was designed to validate the projected shadow of voxel based cloud representations, which required binary information. It also displayed some weaknesses in the segmentation. Those weaknesses are going to be discussed.

Mentioned weaknesses are displayed for the orthogonal image in figure 14 with an example.

Figure 14: Merged orthogonal image with previously existing settings and calibration parameters. Two weaknesses are marked exemplary. Red boxes display the NaN area while the green box contains an example for the offset at the images borders

One problem is the camera calibration, whose effect is displayed in the green box. The calibration appears to be potentially erroneous, since the image borders of the two shadow cameras do not fit to each other. The offset is caused by two images merged in the overlapping area. If the camera model was perfect, the image's borders would not be noticeable in the orthogonal image, since the pixel coordinates would be definitively assigned. The border areas also appear blurred, since they are defined by two cameras and interpolated bilinearly afterwards (see section 2.6). This potentially generates errors, since a shadow's border appears blurred in this area as well. So, it would be beneficial for the shadow detection, if the border areas were clearer. The red area marks the second main problem with the old system. To generate shadow information, only two cameras were used. Combined, they enabled a field of view of roughly 140° on the east side CESA-1. The covered area is therefore enlarged, by adding four more cameras to the system. Also, the displayed image covered an area of $781 \cdot 1369$ square meters. These settings need to be changed, so that the entire PSA is described by pixel information. These problems are going to be solved in sections 3.2 and 3.3.

To display the weaknesses of the system's segmentation, an exemplary segmentation result from [18] is shown in figure 15.

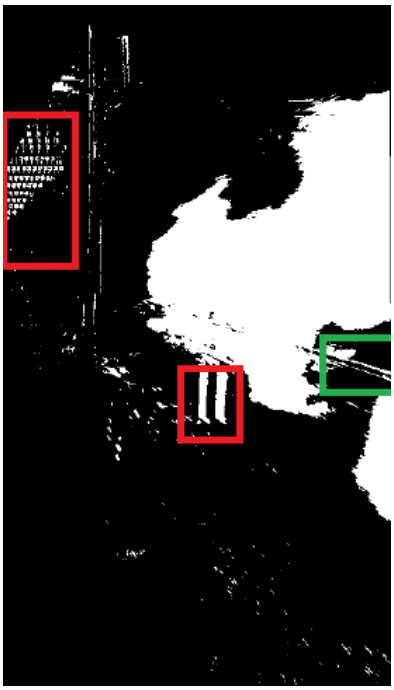

Figure 15: Segmentation result with previously existing system. Two weaknesses are marked exemplary. Both colored boxes display reflective objects. Red boxes display heliostats respectively parabolic collector systems. The green box displays a reflective building, which distorts the segmentation

This image displays the mentioned reflective objects. Those are able to be cleaned from the image, which is enabled by those objects being detached to the shadow. If the objects are not attached to the shadow, they can be determined as small objects and therefore cleaned off. This is potentially erroneous for the detection of the shadow's shape. If those objects were attached to the shadow, they would not be cleaned off and the shadow's border would be distorted. Therefore, they will be excluded as explained in section 3.3.1. The problem, marked by the green box, is caused by a reflective building, which is in the far distance. The reflection causes problems during the segmentation and distorts the segmented shadow. Also, the information gathered is binary, since only one threshold is used. Values above are set to one, while the remaining are set to zero. This does not display the shadow's structure, which is required for the detection of irradiance sensors in section 5.4. It also excludes parts of the shadow, since the used threshold applies for deep shadow regions. Deep shadow regions are going to be defined by their pixel difference. These changes to the segmentation will be applied in section 4. The pixel difference is only used to apply one threshold (see equation 20). Moreover, the images used for segmentation need an adjustment to their color channels. Images taken by the cameras are converted into the sRGB as explained in 2.4.2. Therefore, their pixel values do not display the incident light's value to the CMOS sensor correctly. For the determination of irradiance

maps, a second pixel difference between an entirely shaded and the reference time stamp needs to be applied for the application of the in section 5.3 mentioned methodology.

3.2 Camera Preparation and Calibration

The first step of the system enhancement was to install four additional cameras and to orientate the six cameras such, that a 360° surround view from the CESA-1 tower was obtained. To use the camera information, two calibration processes have to be applied to the existing and the four newly installed shadow cameras. The previously existing calibrations have to be renewed, since the corresponding shadow cameras were moved from their original position to ensure a 360° view around the CESA-1 power tower. Therefore, their exterior orientation do not apply to the new position. The inner calibration is going to be renewed as well, since it is preferred for all cameras to have calibrations of the same methodology, applied by one person, to ensure the homogeneity of created calibrations.

3.2.1 Installation and Adjustment of Shadow Cameras

Four new cameras are positioned onto the CESA-1 power tower at PSA. Each hemisphere is covered by two cameras, except the northern. This direction can not be covered by cameras, since there are heliostats to reflect the incident light onto receivers. The caused heat could therefore endanger cameras in that direction. The area is supposed to be covered by the northern directed cameras of the east- and west-side. Also, the existing cameras were moved, to cover a wider area, since the overlapping area between blurred a potential shadow information. The cameras are identified by the tower's hemisphere they are directed to and the direction it is observing. The east-north camera for example, is placed on the eastern side of the CESA-1 and observing the northern part.

All camera's raw images are displayed in appendix A.1, while their positions on PSA are displayed in appendix A.2.

3.2.2 Determination of the Interior Orientation

The inner orientation parameters $H' = (x'_0, y'_0)$, c and $\delta x', \delta y'$, described in section 2.5.2, are determined by using the Scaramuzza OCamCalib Toolbox for MATLAB [24]. The calculation using [14] was not applied, since the radial symmetric distortion is only compensated up to two thirds of the image radius. But the strongly barrel shaped distortion of wide angle cameras require a different approximation.

The toolbox requires some preparation before the actual parameters can be defined. It needs a checkered pattern (see appendix B), of which a magnitude of photos has to be taken. The pattern is placed on a solid base and moved through the the entire image area,

so that every coordinate of the image was described at least once. It is important, that the checkered pattern is not shaded, because this otherwise would lead to mistakes during the evaluation. Also, the whole pattern needs to appear on the image, since the program is counting the displayed squares respectively their corners afterwards. Consequently, 120 images were taken for each camera. An example for an image taken is displayed in figure 16.

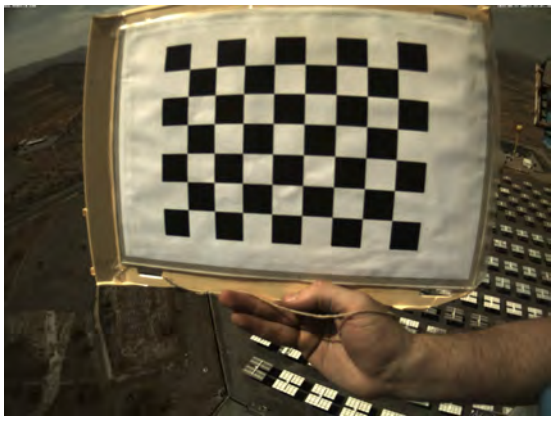

Figure 16: Example for a photo of the pattern , taken from the west-north camera.

The image displays the mostly radial symmetric distortion, visible for the bare eye. While the image center displays barely distorted squares. The distortion rises with the image radius, as visible in the upper image area.

After the initial calibration, the initial average pixel error for all images and all average pixel errors for each picture is determined. To optimize the initial result, all images with average error greater five pixel are sorted out. It also has to be checked, whether all image areas are covered by the checkered pattern. The calibration result is considered successful, if the average pixel error over all images is less than two pixels. The calibration results are displayed in table 2.

Camera	x'_0 / pixel	y'_0 / pixel	c / m	a_0 / -	a_1 / -	a_2 / -	a_3 / -
EN	790.3	1031	0.022	-1232.8	0	$3.002 \cdot 10^{-4}$	$-1.200 \cdot 10^{-8}$
ES	777.2	1063.6	0.022	-1248.1	0	$2.756 \cdot 10^{-4}$	$4.439 \cdot 10^{-9}$
SE	741.8	1051.1	0.022	-1248.2	0	$2.694 \cdot 10^{-4}$	$1.599 \cdot 10^{-8}$
SW	774.1	1004.8	0.022	-1199.4	0	$2.275 \cdot 10^{-4}$	$5.413 \cdot 10^{-8}$
WS	777.8	1021.5	0.022	-1238.4	0	$2.252 \cdot 10^{-4}$	$6.493 \cdot 10^{-8}$
WN	780.8	1038.6	0.022	-1233.3	0	$2.499 \cdot 10^{-4}$	$3.268 \cdot 10^{-8}$

Table 2: Calibration results for all six shadow cameras, installed on the CESA-1 tower.

3.2.3 Determination of the Exterior Orientation

To determine the exterior orientation parameters X_0, Y_0, Z_0, κ, ω and φ from projection equations (section 2.5.3) a numeric system was already available at Deutsches Zentrum für Luft- und Raumfahrt (DLR) for this thesis. To determine the mentioned parameters, features in the displayed image have to be set first. It is beneficial to take images, obtained when no shadow fell on PSA, for the definition of features in the image, since the position of objects is clearer. These features need to be remarkable, so that they can be definitely assigned to one specific pixel in the image. Possible features are edges of buildings, stones, carports, heliostats or crossroads. During the definition of features, it is important for them to be evenly spread over the entire image area. However, a tremendous part of the image area does not contain any characterizing features. If there are image regions which are not covered by any features, the camera does not have any supporting points for these regions. This will be essential for the determination of the exterior orientation parameters. If all points are defined, their GPS coordinates respectively their object coordinates have to be defined as well. To gather the information, Google Earth was used. It might seem inaccurate to use a freeware tool to gather detailed information about the exact position of a coordinate in the open field, but its accuracy was compared to coordinates, which were measured by handheld GPS devices, and considered accurate. The longitude and latitude values differed in the dimension of three meters [4] and was therefore in the range of the uncertainty of an actual GPS measurement. Also, there are problems with metallic structures during the GPS measurement, which is problematic for the determined features. Beside the fact, that the differences are considered acceptable, this tool contains some benefits to GPS devices. While the coordinate for X and Y are relatively consistent, the height coordinate of GPS devices is also inconsistent, according to [4]. Indeed, for this system it is required to have a consistent display of the Z coordinate as well. Also, the availability of Google Earth generated information is of high value, since many features are going to be determined. Therefore, the dynamic determination of Google Earth generated information, independent from the operating person's position or day time, is highly beneficial.

Since the differences between GPS devices and Google Earth are considered insignificant and other benefits from Google Earth outweigh the benefits of GPS devices, the usage of Google Earth was considered properly for this system.
129 evaluable features for the entire area are defined (133 in total but 4 are exceeding the image borders). Figure 17 displays the gathered features.

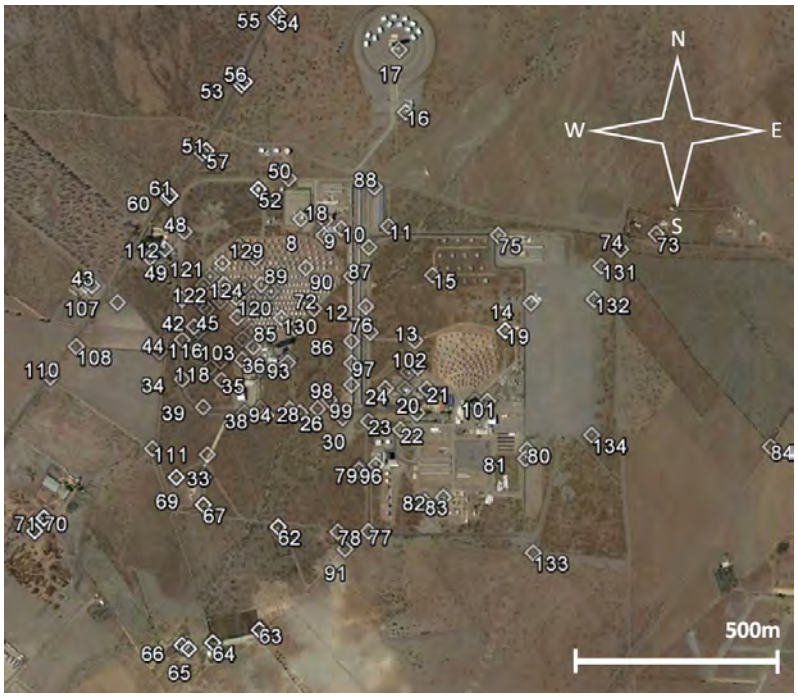

Figure 17: GPS coordinates of features defined in Google Earth, ©Google Earth

Before the actual determination process can be started, the initial camera positions X_0, Y_0, Z_0 have to be set as starting values for the optimization. X_0 and Y_0 cannot be read out in Google Earth due to the parallax. The view onto relatively high objects, like the CESA-1 power tower, is distorted in Google Earth. Only both eastern camera's positions were able to read out. Still, even their position cannot be determined exactly. The other camera's coordinates for X_0 and Y_0 need to be be determined by defining a relation between a known distance and the changing distance in degree. This has to be executed for longitude and latitude, since they are scaled differently. The factor was determined by documenting the change of degree in longitude and latitude for a defined distance. The reference distance was the diameter of the CESA-1 tower which has a cylindrical shape. The diameter is known to be 10 meters. The change of longitude for this distance is $1.702{\cdot}10^{-4}$ degree and the change of latitude is $0.93{\cdot}10^{-4}$ degree. The scale factor for longitude is therefore $0.702{\cdot}10^{-4}$ degree per meter and the latitudes scale factor is $0.093{\cdot}10^{-4}$ degree per meter. The height information is documented for the solar receivers of the CESA-1 tower in [19]. Since the cameras are installed to a handrail on a platform, the initial height of 85 meter was corrected to the estimated height of 87 meter. Moreover, the height information is referring to ground level. Therefore, the total height above see level is 587 meter for all six cameras. In contrast to previous calibration processes, when only the rotation parameters were optimized, the translation parameters (X_0, Y_0 and Z_0) are optimized as well, since the determination of this coordinates also

displays uncertainties. The initial position is displayed in table 3.

Camera	X_0 / °N	Y_0 / °E	Z_0 / m
East-North	37.09491	-2.36123	587
East-South	37.09491	-2.36123	587
South-East	37.094822	-2.361214	587
South-West	37.094822	-2.361217	587
West-South	37.094864	-2.361258	587
West-North	37.094867	-2.361258	587

Table 3: Initial camera position

Afterwards, the GPS coordinates have to be assigned to pixel coordinates, to obtain an affiliation for all pixel coordinates the image displays. This is realized by identifying the affiliations within the raw image's pixel and the coordinates it contains. With the knowledge about the interior orientation and the projection equation (see section 2.5.3), it is possible to project the given global coordinates into pixel coordinates. Moreover, the detected features are assigned manually in the photo to determine the expected position in the image. The manually assigned (red) and projected features (green) are exemplary displayed in figure 18, which shows the initial orientation result for the given parameters, exemplary for the south-east camera.

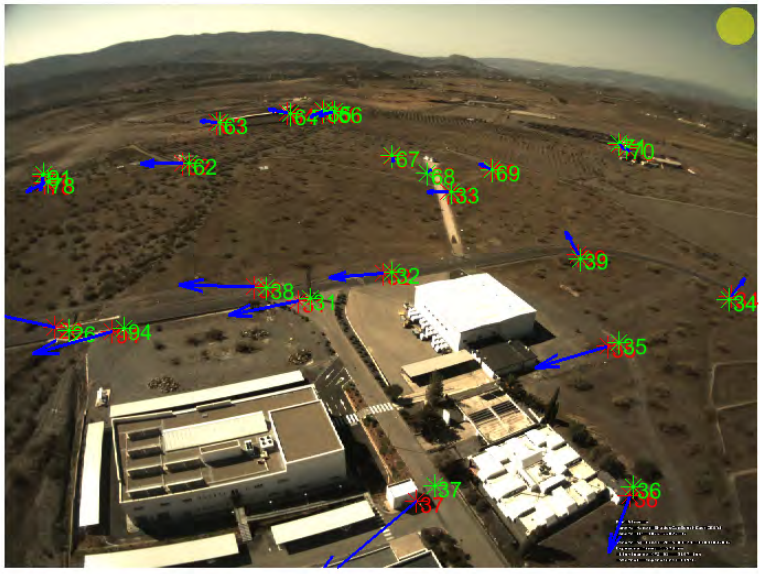

Figure 18: Projection of features (green) with the determined features (red) for the initial configuration of south-east camera. Residuals are drawn between features(blue) Initial deviation: 10.30 pixel

Residuals are drawn to display the deviation . The deviation is shown in an amplified way to enable the relation of the distance between two assigned points, compared to other pairs. The deviation is defined as the root mean square of all appearing residuals. This figure also displays the deviation between the projected feature coordinate and the manually assigned feature position by displaying the deviation with a scale factor, based on the appearing deviation. The length of the drawn vectors is relative to the maximum distance between two assigned points.

All projected coordinate's vectors are intercepting in the projection center. The determined projection center's position differs from its optimal coordinates, which is going to be defined by the minimization of the residuals. The optimal projection center is defined by the position of the manually assigned pixels (red) and the camera model including the interior orientation. Therefore, the remaining distances between manually assigned and projected features have to be minimized. For this reason an optimization process is determining the optimal exterior parameters for the given set of features. The genetic optimization is carried out within bounds, which define the range, in which the optimization is operating. Ultimately, the parameter set with the minimal residuals is the result of the optimization. An exemplary result is displayed in figure 19.

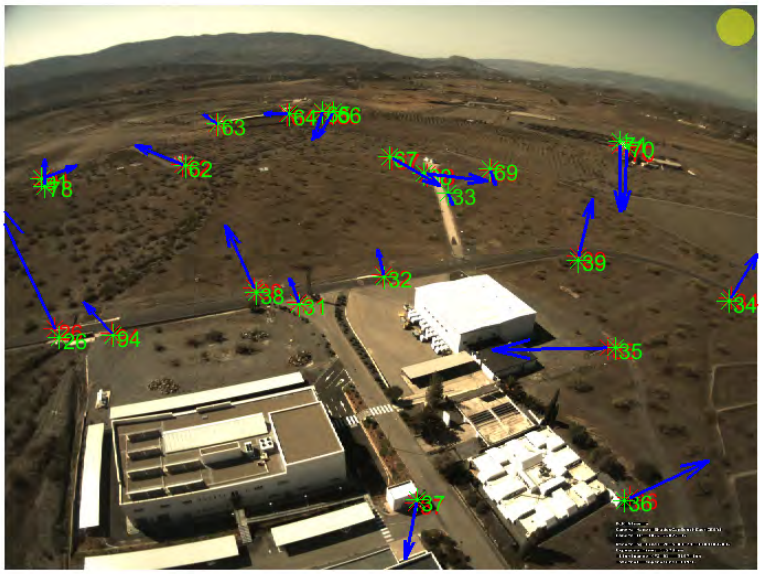

Figure 19: Projection of features (green) with the determined features (red) for the final configuration of south-east camera. Residuals (blue) are drawn between features to display the deviation. Final deviation: 5.20 pixel

The orientation's quality rises by minimizing the residuals root mean square. Besides, it rises with the amount of features detected as mentioned in [14], since there are more

vectors to define the projection center. To optimize the projection center's parameters, an analysis of the parameters is recommended. If there are parameters, which are close to the determined bounds, it is possible, that the optimization of the camera's position can still be improved. Therefore, the mentioned homogeneity of feature distribution is required. Each raw image contains 21 up to 39 significant features to determine the exterior parameters. There are uncertainties in the process, since the pixel coordinates are manually detected and the exact determination of a pixel from an image to the projected coordinate in Google Earth is also containing errors. Therefore, the homogeneity of the feature's spatial distribution should always be valued higher than a lower root mean square value of residuals. The results of the optimization for the orientation of all cameras is displayed in table 4, while the orientations accuracy will be discussed in section 6.1.

Camera	EN	ES	SE	SW	WS	WN
ΔX_0 / m	5.90	-089	-3.86	-0.85	-1.19	-6.1
ΔY_0 / m	-1.48	-3.42	-1.00	-1.43	-0.37	2.51
ΔZ_0 / m	-2.38	-0.34	-1.08	0.11	-0.81	-2.72
ρ / rad	0.911	2.348	2.102	2.970	0.391	1.004
θ / rad	5.678	3.864	2.754	2.158	0.977	1.004
ϕ / rad	4.313	5.308	4.532	3.409	5.805	4.985
Deviation / pixel	± 6.7	± 8.3	±5.2	±8.2	±9.2	±7.5
Number of Features / -	21	35	23	29	31	39

Table 4: Orientation results for all six shadow cameras (directions abbreviated), installed to the railing of the CESA-1 on the PSA. Calibrated on the 29th of January, 2016

3.3 Creation of the Merged Orthogonal Image

Images taken by cameras are distorted by the tilted perspective and the landscape's differences in altitude. By defining orientation parameters, that are obtained in section 3.2, and the application of projection functions (see section 2.5.2), it is possible to project the pixel coordinates to the ground, so that a plain view results. The distorted image is called "orthogonal image" respectively a "to scale representation of the raw image" as seen in [14].

Since the image is a to scale representation of the ground, its scaling is stated in square meter per pixel. The covered area is enlarged, since the evaluation of the entire area of the PSA a bigger field of observation was required. The area observed was enlarged to a field of $2000 \cdot 2000$ square meters in this thesis by adding the four new cameras to the system and readjusting the previously existing cameras. Besides, the orthogonal images

scaling increased to 25 square meter per pixel to reduce the calculation time. This results in a grid size of 5 meters.

All orthogonalized images overlap at certain points, so that all pixels can be associated to global coordinates. Since every point's position to the global reference system is known, and the assignment between global and pixel coordinates is set, the area can simply be enlarged by adding more pixel coordinates, as long as the external and internal calibration parameters are known. In overlapping areas, some global coordinates are assigned to multiple pixel coordinates. The pixel information in this area is interpolated bilinearly in each channel (see section 2.6).
To gain more evaluated area, more pixel coordinates have to be assigned to the existing global coordinates. That way, the area shown in figure 12 was enlarged to the new merged orthogonal image, which is displayed in figure 20. Since the tower's area and also the area close to the tower is not covered by any cameras and therefore not described by any pixel information, there is always a small NaN area left. Also, artifacts appear, due to erroneous image information.

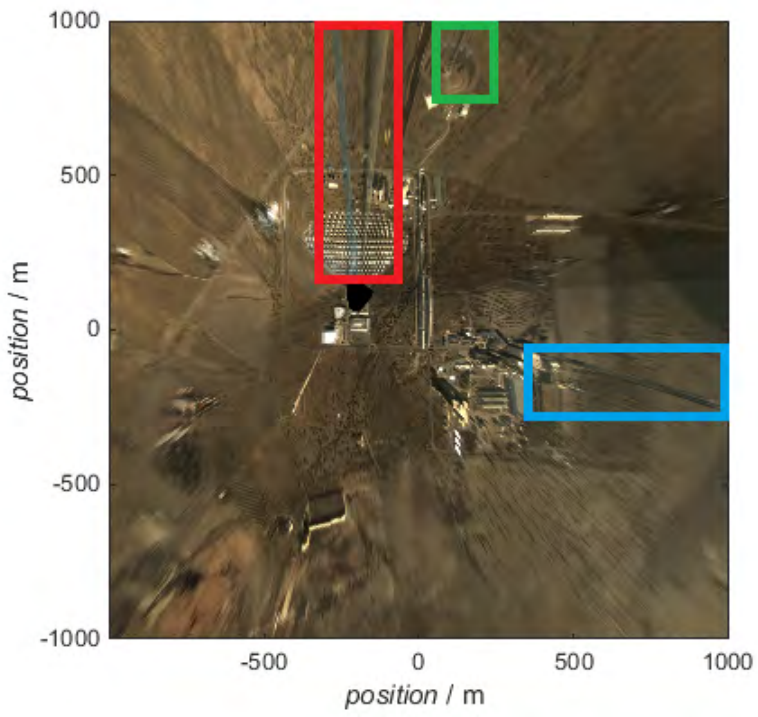

Figure 20: Orthogonal image created by merging images from six cameras, using the new calibration parameters from section 3.2. Some artifacts are marked in red green and blue boxes, which are partially caused by objects reaching into the camera's view or overlapping areas (see section 3.3.1)

3.3.1 Exclusion of Irrelevant Objects

The image still contains a lot of artifacts, which are partly caused by objects, that are relatively close to the camera (red). Besides, high objects appear to be stretched, since there is no information for the area behind them (blue, green). The reason for these artifacts is displayed in figure 21 Furthermore, the overlapping areas, for which two cameras deliver information, are blurred, since the sRGB values are just determined by interpolating each color channel. Also image regions, that are far away from a camera's image center, are more distorted, even after the calibration, which is a typical behavior of distortion [14]. This is caused by radially symmetric distortion as mentioned in 2.5.2. Therefore, it is advantageous for an exact display of the area, to use the pixel information of those cameras, which display the smallest distance to the image center for mentioned pixel.
To accomplish the exclusion of erroneous information, it is required to apply masks to the raw images.
Despite the overlapping regions, every camera is covering a different area of PSA. These erroneous effects are caused by objects that are reaching into the image area or objects, that are relatively high and need to be excluded. The process of excluding parts of the image is exemplary shown for the east-north camera in figure 21.
In figure 20 there are obvious artifacts, caused by mentioned problems. These occurrences are partly the result of the east-north camera's raw image. The image with its corrupted area and the solution to counter these erroneous information are displayed in figure 21.

Figure 21: Raw image from east-north (left) the area, that has been excluded (right)

There is a part of a bar, which is part of the CESA-1 tower's framework. Besides, the railing is protruding into the image area (1). There are multiple concepts of tower power plants installed at PSA. Thus, objects like AORA's Tulip^{TM} system (2) or the tower of Centro Tecnológico Avanzado de Energías Renovables (CTAER)(3) have to be excluded as well. Also, the Small Solar Power Systems (SSPS) tower is excluded, which is not displayed in figure 21, but visible in figure 20 (blue box). As mentioned above, outer

parts of the images have to be cut out as well. While the left area is already cut out due to the railing, the right part still delivers potentially erroneous information due to image distortion (4). Preferably, every global coordinate is defined by one pixel, which is defined by the camera with the smallest distance to its image center. Ideally would be a system, that defines pixel coordinates, with cameras, that are heading into the almost same direction.

There is a region between rod and railing which could be used, but since it is covered with image information of the west-north camera, this region is also removed. The text field was placed in the top left corner, since the horizon does not contain any data, that are evaluated in this process.

There are also effects during further processing, which have to be excluded in the raw image. During the segmentation (see section 4), areas, that are known to be reflective, need to be excluded as well. Thus, the exclusion of reflective areas is also applied during the image creation. During the following segmentation each pixel will be compared between two time stamps of time as introduced in section 2.6.

3.3.2 Resulting Orthogonal Image

After the determination of camera parameters and the application of masks to raw images, the orthogonalized image results as shown in figure 22.

Similar to towers in the closer distance to the camera, objects, which are far away from the cameras, also cover the area behind them. The further mentioned objects are away from the center, the lesser their height has to be, to cover the same area behind them. This also means, that big objects in the far distance are covering tremendous parts of the area. The effects of small objects in the far distance are not considered crucial and the area mainly displays small objects. Still, this causes a difference in orthogonal image compared to satellite images. These images are the basis of segmentation that will be explained in the following. They are from now on described with S_{sRGB}.

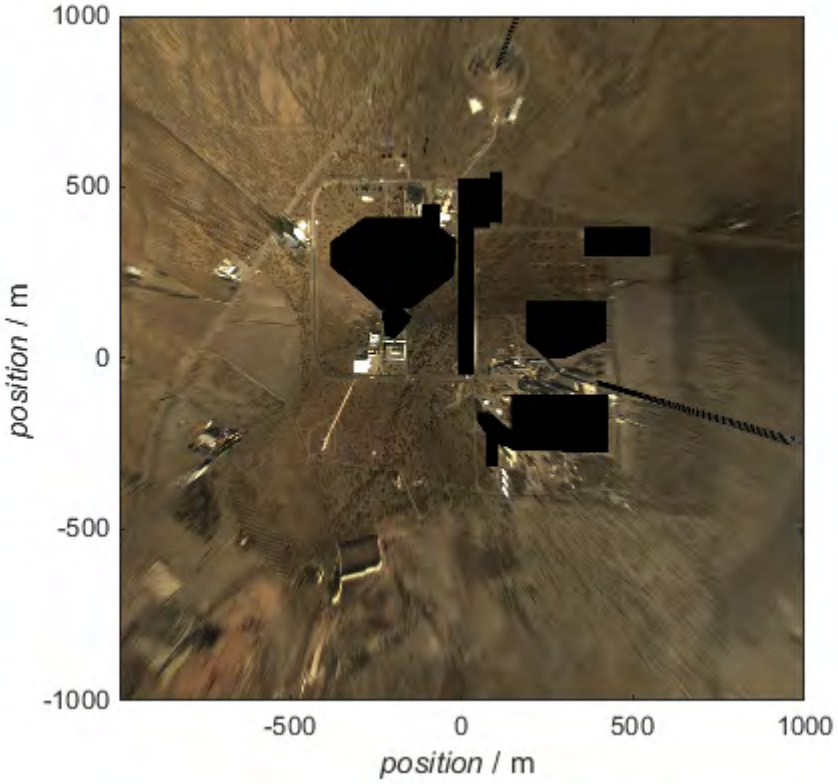

Figure 22: Merged orthogonal image with new calibration parameters and masks for raw images as well as orthogonal image applied - PSA 20.09.2015 11:00:00, UTC +01:00

4 Image Segmentation to gain Shadow Information

The segmentation process provides information about the differences between the shadow condition for the investigated time stamp and perfect, respectively shadowless conditions.

To accomplish this, the grayscale image of S_{sRGB} has to be determined. Also, the image has to be normalized, to strengthen the segmentation against alternating SZAs. The pixel value difference, compared to shadowless conditions, is defined for an exemplary time stamp with non linearized grayscale images. The shadow's structure is processed, by applying multiple global thresholds to the resulting pixel difference. Global thresholds are determined, by using a histogram analysis of the difference image.

For the procession of the segmentation and ultimately the irradiance map creation in section 5, an exemplary time stamp is presented in the following. The chosen time stamp is the 19th September 2015, 12:57:00, UTC +01:00.

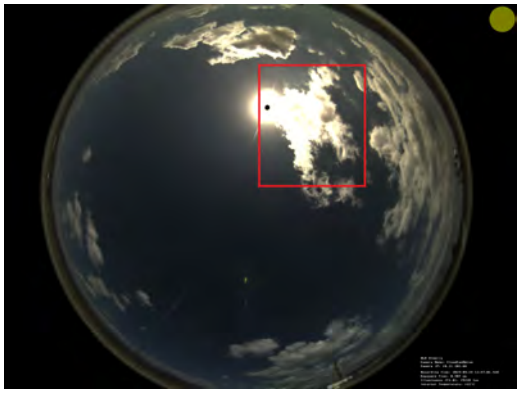

Figure 23: Cloud, whose shadow has to be segmented (red box) in orthogonal images. View from WSI 19.09.2015 - 12:57:00, UTC +01:00

Figure 23 shows the cloud, which is causing a shaded area on PSA, from a WSI. The actual segmentation is processed with orthogonal images. This figure displays the cloud that causes the introduced shadow.

4.1 Shadowless Events

For the segmentation, shadowless events, generated by WSIs, of a 20min interval are used. It is divided into 10min intervals around the investigated time stamp. This period was doubled, compared to the previous settings. Previously, it was only possible to get shadowless events from the past, which is still the only way to process shadow camera data in real time. While processing time stamps of the past however, shadowless events from the closer future are also taken into account. The sun's position is not changing significantly within ten minutes, which means, that shadows on the area of PSA, caused by

static objects, are not changing significantly, either. Consequently, they are not detected as a difference from the investigated time stamp. Furthermore, it is assumed that the area's reflective properties are not changing significantly within ten days. Therefore, the segmentation also uses time stamps, which are inside the defined interval on closer dates of the future as well as the past. These time stamps define $S_{\text{ref,sun}}$ in the further process.

4.2 Difference Value Image

For the creation of the pixel difference image, grayscale images are used (see section 2.6). There are multiple options, to determine the grayscale value of an image. For this process, the mean average of the three color channels was build, as seen in [21]. S_{sRGB} is a exemplary non linearized image pixel of all color channels. Equation 22 applies for all pixels in the image.

$$S_{\text{gray}} = \frac{S_{\text{sRGB}}(R) + S_{\text{sRGB}}(G) + S_{\text{sRGB}}(B)}{3} \tag{22}$$

S_{gray} is the grayscale image and will be referred to as S, since only the grayscale values are processed.

Considering that the sun is rising and setting throughout the day, shadows on the area change, depending on SZA. For the existing definition of the difference image, the pixel value difference can differ throughout the day and especially throughout the year. Considering that global thresholds are going to be applied, a normalization of the difference image is required, so that the derived pixel differences are displaying similar values throughout the year. It is realized by dividing $S_{\text{ref,sun}}$ and S_{Eval} by the 75th percentile N_{75} of the reference image. The 75th percentile displays a defined value, that is greater than 75 percent and smaller or equal to 25 percent of the appearing values in $S_{\text{ref,sun}}$. Thus, the segmentation is less vulnerable to changing irradiance conditions, especially for evaluations of images taken in the morning or in the evening. After the normalization the pixel difference is given by

$$S_{\text{diff}} = \frac{S_{\text{ref,sun}}}{N_{75}} - \frac{S_{\text{Eval}}}{N_{75}} \tag{23}$$

The normalization is followed by a cleaning process, which excludes small areas, that are considered erroneous information, defined by the cluster size from the area. It occurs, that areas of the analyzed image appear to be brighter than the reference image. Since only the difference in shadow information should be segmented, while the reference image contains ensured shadowless conditions, negative differences are set to zero. The shadow-

less orthogonal image and the investigated time stamp are displayed in figure 24, while the non linearized difference image, cleaned from small clusters, is displayed in figure 25.

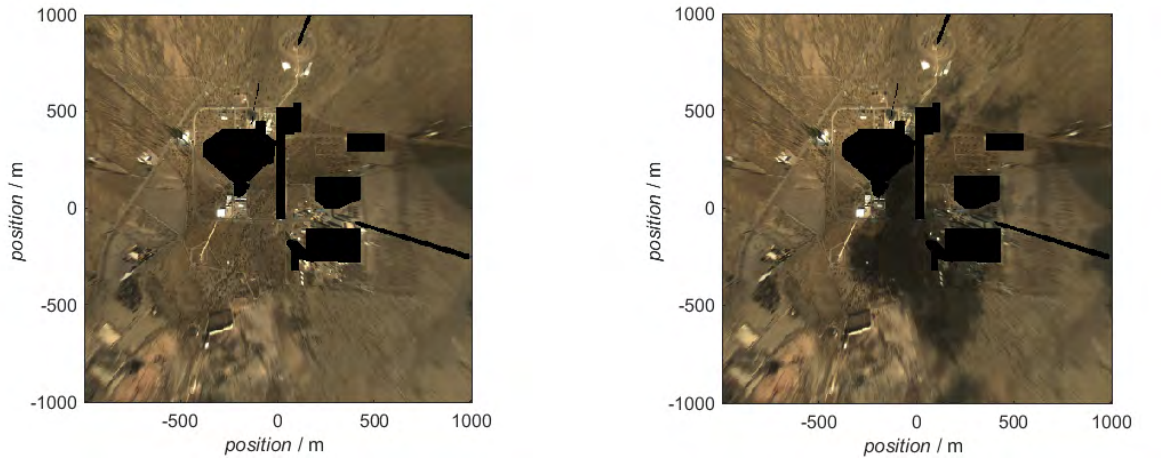

Figure 24: Reference image $S_{\mathrm{ref,sun}}$ (left) and the investigated time stamp S_{Eval} (right), 19.09.2015 - 12:57:00, UTC+01:00

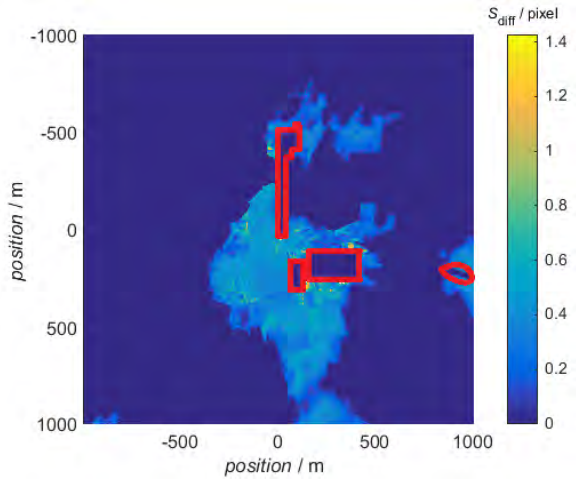

Figure 25: Non linearized pixel difference image S_{diff}, 19.09.2015 - 12:57:00

4.3 Determination of Thresholds

For the application of thresholds, the non linearized pixel difference is used. In the previously existing system, one threshold was used. It couldn't gather all required information about the shadow's structure. In fact, there have to be multiple indicating areas, to describe the shadow. In figure 25, NaN areas are visible (red boxes). Since these values for orthogonal images are not evaluable, they are not defined in both images and therefore, there is no information about the pixel difference in this area. Second, the ground information can be seen in the image as well. Mainly dark parts of the PSA area cannot be

segmented correctly, since these areas absorb more incident irradiance. Therefore, there are sprinkles in the surface of the shadow information. Besides, there is an area close to the PSA, which is planted with trees (see figure 24 left and right), that are barely reflecting any light to the camera sensor. Thus, the pixel difference in this area is constantly lower than the area around them. Moreover, there are areas in the image, which are specularly reflecting the irradiance to the camera sensor. These area's pixel differences are significantly higher than the values around then. Ultimately, they appear as spikes in the difference image. Also, there are erroneous effects, which can appear as a veil. Those are the result of the reflecting influence of CSP plants.
After the application of thresholds, the shadow's structure needs be recognized. To determine global thresholds, the following methodology is used. A histogram analysis is used, to gain information about the pixel differences frequency distribution. By doing this, it is possible to create layers within the shadow, which contain different criteria, that are crucial for later processing.

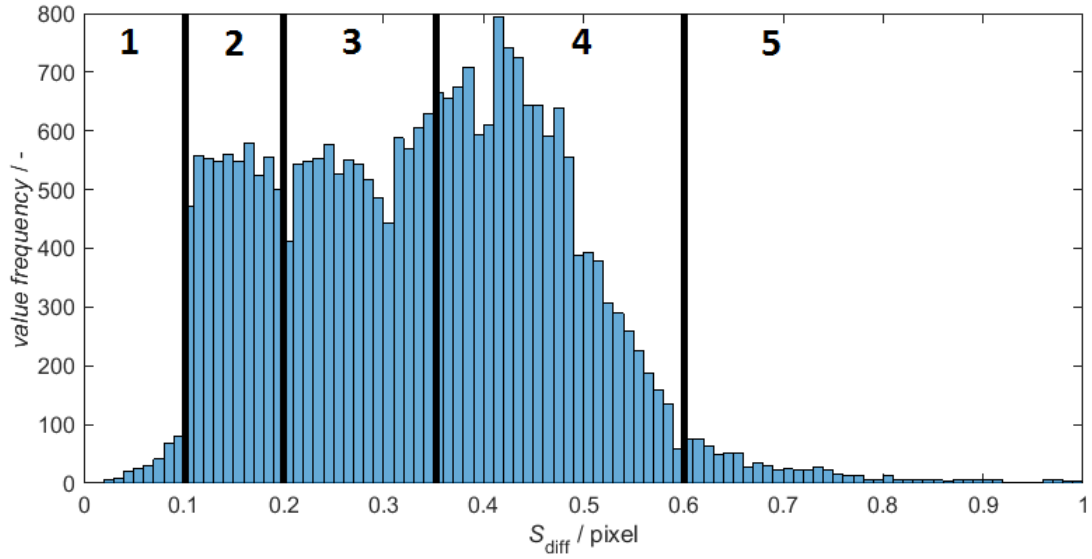

Figure 26: Histogram of non linearized pixel difference S_{diff}: 19.09.2015 - 12:57:00, UTC+01:00

Figure 26 displays the values' difference frequency, dependent on their appearing value. While watching at the appearing differences, it is conspicuous that there are five intervals, which are defining areas in the difference image. Three intervals are describing the shaded area, while two are describing remaining erroneous effects.

Unchanged pixels describe pixel value differences, that are lying beneath the smallest threshold (1). These differences appear mostly because of sunny of dark areas.

Reflections are spikes, which appear as mentioned before (5). These values also do not

generate any information about the shadow.

Shadow which appears to be a cluster of difference values, that are connected to each other as seen in the figure 25 (2,3,4). The shadow itself has to be departed into two parts, since a differentiation between light and dark shadow required. Also, there is an area referred to as "probably cloud" (2). It displays small difference values, that mainly appear in the outer shadow regions, since the values, generated by these are experienced to be smaller.

In the further processing it is required to know at which point of the shadow the DNI is considered low. These areas are considered to be caused by thick clouds, while the rest of the cloud is considered as "thin cloud" and "probably cloud". Also, a differentiation between the erroneous effects and probable clouds has to be made, since the transition in the histogram is fluent.
The corresponding difference values on the x-axis are determined as thresholds for shadow characterization and mentioned in 5. Besides, they also were indicated logically to generate a mask, that contains detailed information about the shadow's status for each pixel in the image. The concept of generating information was kept, but still the amount of information was increased, since the transferred information contains five logical conditions.

The threshold's values, which are referring to normalized pixels, are displayed in table 5.

Classification	Logical Index / -	Threshold / $\text{pixel}_{\text{norm}}$
thick cloud	0	≥ 0.35
thin cloud	1	≥ 0.2
NaN	2	-
probably cloud	3	≥ 0.1
sun	4	$= 0$

Table 5: Classification of shadow regions with their corresponding logical indices and thresholds for S_{diff}

Displayed thresholds are only determined once. The histogram was an exemplary display of their application. By applying multiple thresholds to the difference image, a quinary (*containing five*) map results, that describes the shadow's structure, depending on the pixel values that are contained. The mask is shown in figure 27 and subsequently forwarded to the irradiance procession in section 5.

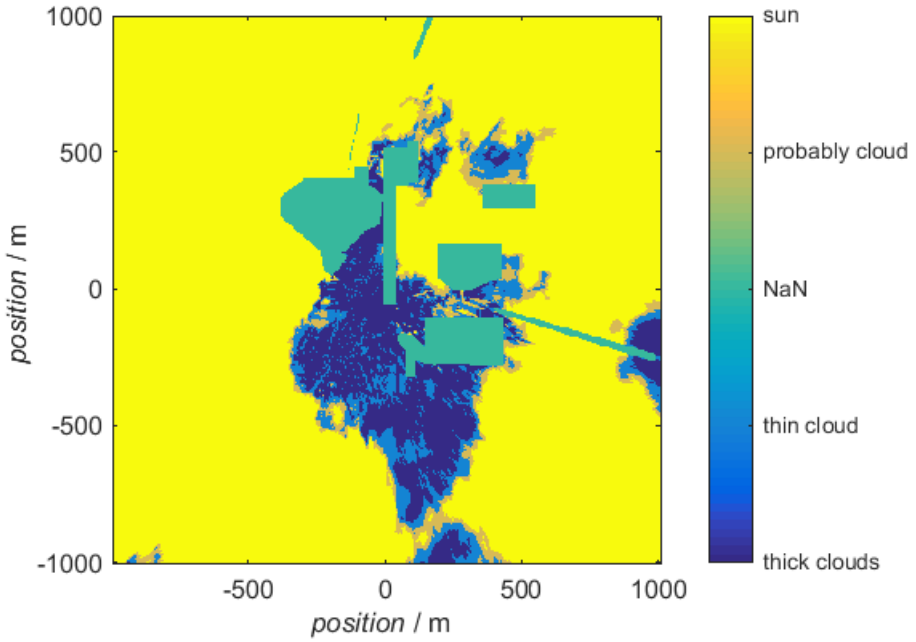

Figure 27: Segmentation result after the application of thresholds to the non linearized difference image 19.09.2015 - 12:57:00, UTC+01:00

5 Combination of Shadow Information and Irradiance Data

Irradiance maps are displaying the irradiance value for the demanded coordinate in the observed area in a given spatial resolution. The measured data of 21 radiometers, introduced in section 2.3, is used for the creation of irradiance maps in this chapter. The data from 20 pyranometers is given in one second averages, while the data derived by the pyrheliometer is saved as ten second averages, because of its thermopile sensor. The data from the pyranometers contain a higher temporal resolution, which is beneficial for nowcasting, since fast changes to the area can be evaluated. Still, the pyrheliometer has a lower uncertainty, compared to the pyranometers. Also, the DHI, which is required for the further irradiance map creation, is measured at the PSA HP station by using a pyranometer with shading device, represented by a tracked shadow ball (see section 2.3). The DHI is used to determine DNI information from the pyranometers. This is accomplished by the relation between the appearances of irradiance, introduced in section 2.2.
The determination of DNI in shaded areas, which are not covered by any sensors, is a major issue for the determination of irradiance maps, covering an area of four square kilometers. To solve this problem, the camera information is used, to add information about the detected shadow and the incident radiation on the ground, seen in each pixel. The combination of the camera's sensors and the actual irradiance measurement devices leads to detailed information about the areas state of irradiance.

The linearization of orthogonal image's color channels will be executed in this chapter, to gain information about the irradiance in sensor coordinate m, n. Afterwards, a reference time stamp, which is entirely shaded, is defined and its pixel difference to a shadowless time stamp is build. These are required for the created model, which defines a relation between pixel difference in grayscale images and the corresponding irradiance for the evaluated area. This evaluation of irradiance data, combined with the segmented shadow information, requires knowledge about the shading of sensors, to assign their measured values to the corresponding shadow information. Therefore, the in section 4.3 derived data about the current shadow position and its profile is used to mark sensors with logical indexes, that define the shadow's depth. This assignment of pixel values to an irradiance allows detailed information about the DNI and GHI condition in shaded areas. Afterwards the implementation of the mentioned methodology is going to be explained, which leads to irradiance maps in the chosen resolution.

The process is displayed in figure 28

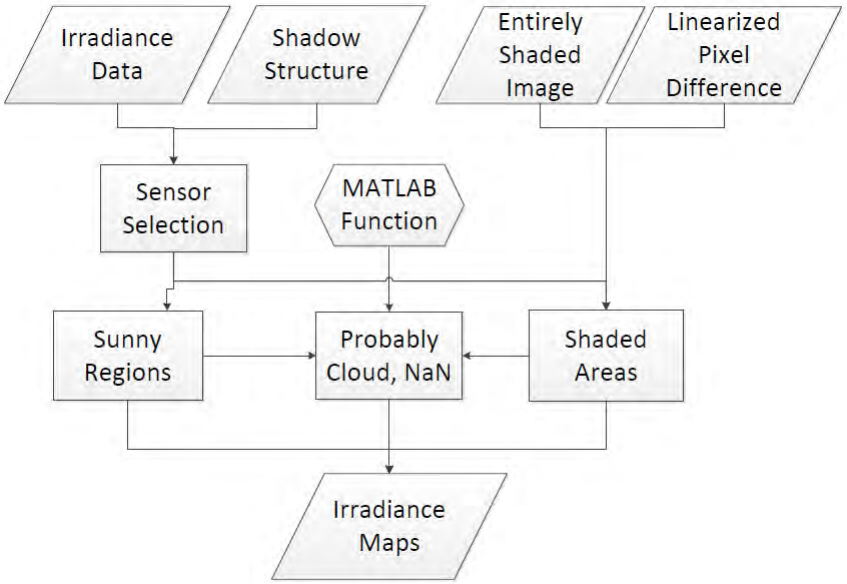

Figure 28: Flowchart for the creation of DNI and GHI maps. Mentioned regions describe the determination of those.

5.1 Linearization of Color Channels

As mentioned in 2.6.1 the CMOS's transformed pixel values S'_{M} is processed with a non linear transfer function internally, to fit to the sRGB conformation [21]. This procedure is called a gamma correction. For the further processing, it is detrimental to gain information about the amount of photons, which the sensor's coordinate m, n received. First of all, the eight bit coded sRGB information has to be normalized to display values in the interval [0,1] as seen in [10]. For sRGB, the factor to be divided by is 255. By doing this, it is possible to determine the corresponding values S (see section 2.4.2). Afterwards, the inverse function of equation 11 is applied to S, to counter the initial gamma correction. For the display of S'_{M}, the index is neglected for convenience.
S'_b with $b \in R, G, B$ is defined as the linearized image value in three color channels. It is defined by equation 24.

$$S'_b = \begin{cases} \dfrac{S}{12.92} & ,if \quad 0 \leq S \leq 0.03928 \\ \left[\dfrac{S + 0.055}{1.055}\right]^{2.4} & ,if \quad 0.03928 \leq S \leq 1 \end{cases} \tag{24}$$

Afterwards, the irradiance has to be computed from S'_b. Since the relation between linearized grayscale images values and the incident irradiance is assumed, the grayscale images are build with the arithmetical average of all three color channels as seen in equation 22.

More beneficial for the purpose of gathering information about the incident irradiance would be a weighted sum of the components energy. However, this definition for equation 22 is mentioned in [21] and considered sufficient for these purposes. Similar to section 4.2, S'_{gray} will be referred to as S' since only the grayscale values are processed. Then, the linearized grayscale images difference S'_{diff} is build analogue to the non linearized pixel difference in equation 23. The linearized pixel value difference S'_{diff} is displayed in figure 29.

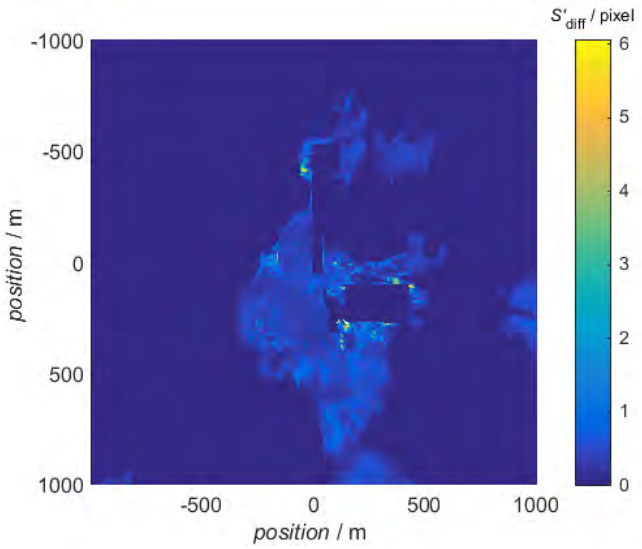

Figure 29: Difference image after linearization and segmentation processes 19.09.2015 - 12:57:00, UTC+01:00

5.2 Reference Shadow

To evaluate shaded regions, that are not described by irradiance sensor information, it is required to define a reference shadow, respectively a reference pixel difference. For the detection of an entirely shaded time stamp, DLR's irradiance measurement database is used. It is possible to retrieve the irradiance for the installed stations. By doing so, it is possible to detect events, that contain close to zero DNI. Besides, the shadow camera's videos of inspected days were used to ensure, that the entire area was shaded. The detected event has to be temporally close to the event, which has to be evaluated, since the pixel information for the coordinate m, n depends on its reflective properties. Exterior influences like rain, vegetation, or generally speaking any change to the optical properties of the observed area influence the result. The entirely shaded time stamp was detected at the 24th of September 2015 at 13:21:00, UTC+01:00 for the exemplary data point. Thus, the pixel difference is defined as

$$S'_{\text{diff,shad}} = S'_{\text{ref,sun}} - S'_{\text{ref,shad}} \tag{25}$$

5.3 Model for the Determination of Irradiance Maps

In section 2.4.2 the composition of a pixel value for the camera's sensor was introduced. Since a gamma correction was applied in section 5.1, the definition of a corrected pixel with $S' = {\Gamma_{\text{sRGB}}}^{-1}(S)$ leads to the modified version of equation 13 as displayed in equation 26.

$$S'_{mn} = M_{\text{cam}} \int_{Amn} \mathrm{d}A \int_{\lambda_{min}}^{\lambda_{max}} \mathrm{d}\lambda \cdot t_{\text{exp}} \cdot \vec{\varepsilon_{\text{N}}} \cdot E_{\lambda} \tag{26}$$

The MasterPed term is neglected since the cameras show zero as pixel values at night for selected pixels. The following assumptions have been applied to the given definition of S'_{mn}.

- The spectral irradiance, which is reflected to the sensor, is homogeneously distributed within the pixel for every single pixel. The integration over the area $A_{m,n}$ is therefore replaced by a constant factor for the pixel m, n
- For every pixel, $\vec{\varepsilon_{\text{N}}}$ is considered constant.

Furthermore it is assumed that the resulting value of grayscale images, after the gamma corrections of every color channel, is proportional to the broadband irradiance at the coordinate m, n. Also, the non diagonal components of M_{cam} are considered insignificant, compared to the diagonal components (see equation 10).
If these assumptions are applied to equation 26, the relation between broadband irradiance and pixel value results.

$$E_{\text{BB},mn} \cdot const_{mn} = S'_{mn} \tag{27}$$

The difference of pixel values for two pictures $S_{1,mn}$ and $S_{2,mn}$ is therefore proportional to the difference of the corresponding irradiance intensities on the ground with the proportional factor $const_{mn}$.

$$S'_{1,mn} - S'_{2,mn} = (E_{\text{BB},1,mn} - E_{\text{BB},2,mn}) \cdot const_{mn} \tag{28}$$

5.3.1 Specification of Spectral Irradiance

$E_{\text{BB},mn}$ is characterized by DHI & DNI for the coordinate m, n and displayed in figure 30.

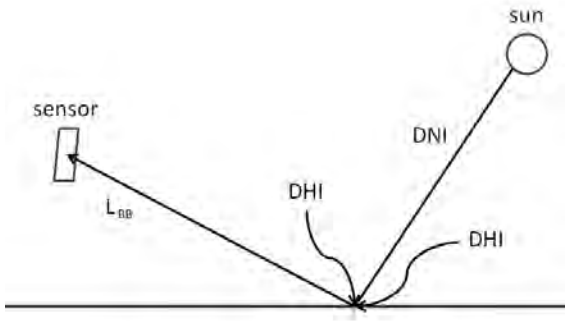

Figure 30: Illustration of spectral radiation L_{BB}, which causes spectral irradiance $E_{\mathrm{BB},mn}$ at sensor coordinate m, n.

$E_{\mathrm{BB},mn}$ in the pixel m, n is composed out of the irradiance, that is reflected towards the camera at the corresponding ground element m, n. DNI and DHI are falling on this ground element. This relation is described in equation 29.

$$E_{\mathrm{BB},mn} = DNI_{mn} \cdot BRDF_{mn} + \sum_{i=1}^{\mathrm{M}} DHI_i \cdot BRDF_{\mathrm{DHI},mn,i} \tag{29}$$

The BRDF (see section 2.1) is describing the ground's scattering behavior and is therefore considered constant for short amounts of time. Also, here the conversion factor from radiance to irradiance for the individual pixel m, n is included in the $BRDF_{mn}$.
DHI is expressed as the sum of i DHI_i from solid angle ,i. The complete upper hemisphere is divided into M such solid angles.

$$\sum_{i=1}^{\mathrm{M}} DHI_i \cdot BRDF_{\mathrm{DHI},mn,i} = DHI \cdot const_{\mathrm{DHI},mn} \tag{30}$$

It is assumed that there is a constant $const_{\mathrm{DHI}}$, which allows the simplification in equation 30. Therefore the spectral irradiance is approximated as

$$E_{\mathrm{BB},mn} = DNI_{mn} \cdot BRDF_{mn} + DHI \cdot const_{\mathrm{DHI},mn} \tag{31}$$

In the ongoing explanation, only broadband irradiance is considered. Thus, the index is not going to be used any further. Afterwards, two pictures are observed, which contain the same SZA and optical properties for the observed ground element m, n. So

$$S'_{1,mn} - S'_{2,mn} = const_{mn} \cdot [(DNI_1 - DNI_2) \cdot BRDF_{mn} + (DHI_1 - DHI_2) \cdot const_{\mathrm{DHI},mn}] \tag{32}$$

applies.

Afterwards it is assumed, that the pixel difference is dominated by the DNI difference. This means that the DHI negligible. So the approximation to the DNI difference at the sensor coordinate m, n results in :

$$S'_{1,mn} - S'_{2,mn} = const_{mn} \cdot (DNI_1 - DNI_2) \cdot BRDF_{mn} \tag{33}$$

In the further documentation every time stamp S'_1 is taken from shadowless conditions, while every time stamp S'_2 is evaluated for shadow information.

5.3.2 Map Composition

There are three different methods for the determination of the DNI values. The method for a pixel influence is selected based on the segmentation's result from section 4.3. These cases are explained in the following.

1. Irradiance measurements for positions, that are segmented with the map index 4, are taken into account, to generate a DNI value that for sunny regions. Hereby it is assumed, that the DNI difference is mainly caused by clouds [12]. Therefore, the DNI maps are giving detailed information about the effects of clouds to the DNI.

2. The values for regions segmented as 0 (thick cloud) or 1 (thin cloud) are determined by using equation 33, solved for the DNI in shaded regions $DNI_{\text{shad},mn}$.

$$DNI_{\text{shad},mn} = DNI_{\text{sun}} - \frac{S'_{\text{ref,sun},mn} - S'_{\text{eval},mn}}{const_{mn} \cdot BRDF_{mn}} \tag{34}$$

3. The border area between both areas (probably cloud, index 3) is interpolated by using the function"griddata.m" from MATLAB, because the sensor information of these regions is considered problematic, which is caused by temporal and spacial deviation in the system. Since there is an uncertainty in the detected shadow coordinates, it is possible, that the shadow is detected on top of a sensor, although it displays values from shadowless conditions. The detection process is going to be explained in section 5.4.

In case 2 (see equation 34), the term $const_{mn} \cdot BRDF_{mn}$ has to be known, to derive the DNI. For convenience, the term $const_{mn} \cdot BRDF_{mn}$ will be substituted by $BRDF'_{mn}$ in the following.
The determination of $BRDF'_{mn}$ is possible from the sunny and the evaluated image for

points of the observed area, whose DNI difference is known. Effectively this applies to the sensor coordinates in the map. For these pixels m, n, $BRDF'_{mn}$ is determined by

$$BRDF'_{\text{sens},mn} = \frac{S'_{\text{ref,sun},mn} - S'_{\text{eval},mn}}{DNI_{\text{sun},mn} - DNI_{\text{eval},mn}} \tag{35}$$

For the determination of irradiance values for an area, where no sensor information is given, the camera generated pixel difference is taken into account. To define the area between the sensor generated $BRDF'_{\text{sens},mn}$, a time stamp was determined, that only displays shaded areas. For the shaded reference time stamp $DNI_{\text{eval},mn}$ is zero. The orthogonal image represents $S'_{\text{ref,shad},mn}$ for this shaded time stamp. By doing so, equation 35 can be used for all image coordinates. The clear sky DNI for this time stamp is obtained from the corresponding shadowless time stamp. It is expressed by the index $_1$. This relation leads to equation 36.

$$BRDF'_{\text{ref,shad},mn} = \frac{S'_{\text{ref1,sun},mn} - S'_{\text{ref,shad},mn}}{DNI_{\text{ref1,sun}}} \tag{36}$$

$BRDF'_{\text{ref,shad},mn}$ map can be defined for every time stamp, by using the pixel difference between the shadowless reference image $S'_{\text{ref,sun},mn}$ and the completely shaded reference image $S'_{\text{ref,shad},mn}$, containing only shadow information, for the currently evaluated time stamp. For the sensor coordinates, two results for $BRDF'_{mn}$ are obtained from equation 35 and 36. In the following, the treatment of these two possibly unequal results is discussed.

If equation 35 and equation 36 are set into relation to each other, equation 37 is obtained, which defines a factor f_{map}.

$$f_{\text{map},mn} = \frac{BRDF'_{\text{sens},mn}}{BRDF'_{\text{ref,shad},mn}} \tag{37}$$

Ideally, this value is close to 1, since the two methods to determine $BRDF'_{mn}$ should yield the same result. The correction factors are obtained for all sensors, that are detected within the shadow. The corrected and final $BRDF'_{mn}$ map should represent the sensor measurement as good as possible, since the ground based measurements are considered more accurate than the purely image based result. To derive an easily applicable correction for all pixels without a sensor, the median $f_{\text{map,med}}$ of all determined $f_{\text{map},mn}$ is calculated. By using the median it is ensured, that outliers, caused by an erroneous segmentation, are excluded. This determines the relation between the DNI in shaded regions for the evaluated time stamp and the pixel differences. The determined correction factor is

applied to the denominator of equation 34.
The shaded DNI for every pixel in the observed area, detected as shaded by a thick or thin cloud, is given by the modified equation 34 as

$$DNI_{\text{shad},mn} = DNI_{\text{sun}} - \frac{S'_{\text{ref,sun},mn} - S'_{\text{eval},mn}}{BRDF'_{\text{ref,shad},mn} \cdot f_{\text{map,med}}} \tag{38}$$

5.4 Sensor Detection

To determine, whether a sensor is shaded or not, the sensor's position is projected onto the area, which is observed. The coordinates of all sensors are measured by handheld GPS devices.
The given GPS information has to be transformed into local system coordinates, defined by the origin, which is the center of the observation. By doing so, the distances of every sensor's position to the origin is given in Cartesian coordinates. Then, the local coordinates are transformed to their closest grid coordinate, since the segmented information, which contains the statement whether the sensor is shaded or not, is only given for the actual grid parameters. Therefore, the logical value for each sensor can be determined. The sensor positions are displayed in figure 31, overlayed with a segmentation result.

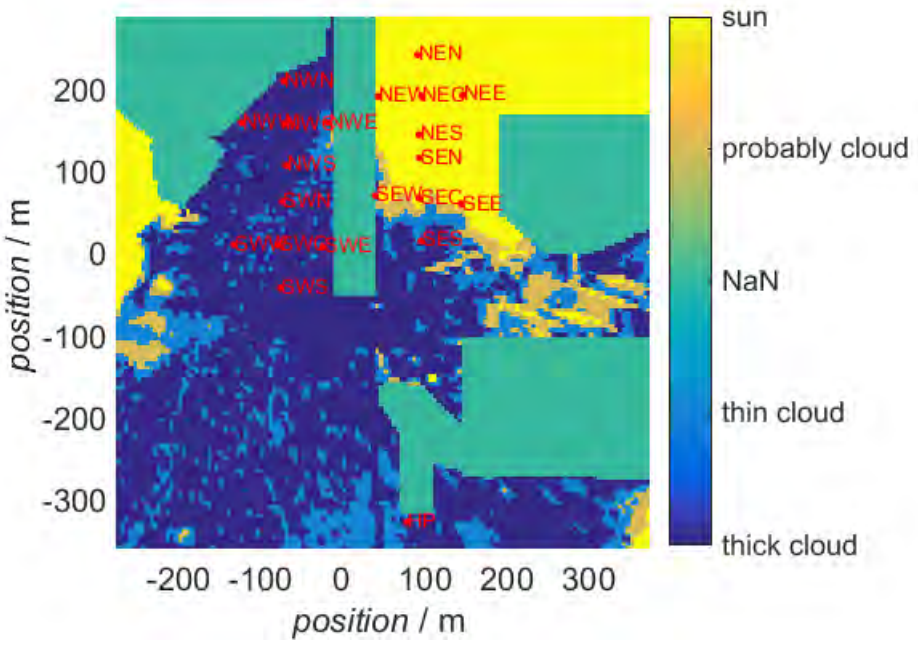

Figure 31: Result of the shadow segmentation for the 19th of September, 12:57:00, UTC+01:00. Including the positions of the pyrheliometer from the reference HP station at PSA in the south. Also indexes are applied to the map, based on their pixel values.

Sensor	Classification / -	E / $\frac{W}{m^2}$	Sensor	Classification / -	E / $\frac{W}{m^2}$
NEN	4	849	SEN	4	698
NEW	4	685	SEW	1	548
NEC	4	821	SEC	4	618
NEE	4	863	SEE	4	593
NES	4	835	SES	0	146
NWN	0	0	SWN	0	0
NWW	0	183	SWW	0	26
NWC	0	0	SWC	0	15
NWE	1	51	SWE	0	33
NWS	0	0	SWS	0	0
HP	0	48			

Table 6: Segmented sensors and their corresponding DNI values for 19.09.2015 12:57:00, UTC+01:00. 0 = thick cloud's shadow, 1 = thin cloud's shadow, 4 = sunny area

Table 6 displays the sensors and their classification, based on the segmentation, as well as their measured DNI for the given time stamp. The initials represent the sensor's position by their direction in the field. So "NEN" represents the grid's north-east-north sensor. The sensors, which were shaded, according to the segmentation in figure 31, are in fact shaded during this period. In general, the segmentation approves, how the sensors were influenced by DNI. Moreover, the sensors, detected in sunny regions, display usual values for clear sky DNI. However, the NWW and SES sensors display values for thin cloud's shadows.

The DNI of course differs throughout the day and reaches its maximum during zenith hours. This maximum value depends on the season and the atmospheric conditions, as mentioned in section 2.2. During January the DNI can reach values greater than 1000 watts per square meter, while during September values up to 900 watts per square meter are usual. The clear sky DNI is derived by all sensors segmented as "sunny". Three of the south-east grid diamond's sensors are detected in the sunny region as well. They still display irradiance values, which appear to be affected by a thin cloud's shadow, since their values are reduced, although there was no shadow detected in this area. This could be caused by an erroneous determination of the shadow's position. Besides, the thresholds could have cut off parts of the "probably cloud" area. Also, their DNI values can be influenced by the direct solar steam (DISS) power plants near to them. During sunrise and the early morning hours, their values can be influenced by reflections from these reflective objects. Furthermore, three of those four sensors, detected as "sunny" display

values of "thin cloud"'s shadow areas.

These effects have to be considered while determining the clear sky DNI for section 5.5. Also, the reflective properties of the area are affecting the result.

5.5 Exemplary Composition of Irradiance Maps

The composition of the irradiance maps is implemented as explained in section 5.3. This requires the clear sky DNI, the determined DNI values for shaded regions and the interpolation between them.

5.5.1 Determination of Sunny Regions

For the definition of the sunny regions it is assumed, that the DNI is dominated by the effect of clouds as mentioned by [1]. Thus, the clear sky DNI is considered constant and set to an average value of sensor's detected as "sunny". Since the sensor detection is considered potentially erroneous, the 90th percentile of all sensors, segmented as "sunny", is build. For the exemplary time stamp, this value is defined as 828 watts per square meter.

5.5.2 Determination of Shaded Regions

To describe the irradiance for shaded regions, it is required to evaluate the in section 5.3 mentioned reference time stamp which displays an entirely shaded area, ideally with no influence of DNI. Therefore, the pixel difference between the clear sky $S'_{\text{ref,sun},mn}$ and the entirely shaded time stamp $S'_{\text{ref,shad},mn}$ was build. To determine the DNI for shaded regions, it is required to define $BRDF'_{\text{ref,shad},mn}$ and $f_{\text{map,med}}$, so that equation 38 can be applied.

5.5.3 Definition of Map Factor, Sensor's and Map's BRDF' Values

The sunny reference was detected at the 19th of September 2015 at 12:52:00 pm, UTC+01:00, while the entirely shaded time stamp was detected at the 24th of September 2015 at 13:21:00, UTC+01:00. The changes to the area of the PSA during this period are considered insignificant. Also the clear sky DNI is considered constant for the entire area.

$BRDF'_{\text{sens},mn}$ is determined, using equation 35 with the clear sky DNI_{sun} for this time stamp, which was measured as 828 watts per square meter. The sensor's factors $f_{\text{map},mn}$ can only be determined for those pixels, which are actually shaded. As seen in table 6, 11 sensors are detected in the "thick cloud" area.

To determine the $BRDF'_{\text{ref,shad},mn}$, equation 36 was used. The resulting $BRDF'_{\text{ref,shad},mn}$ is displayed in figure 32.

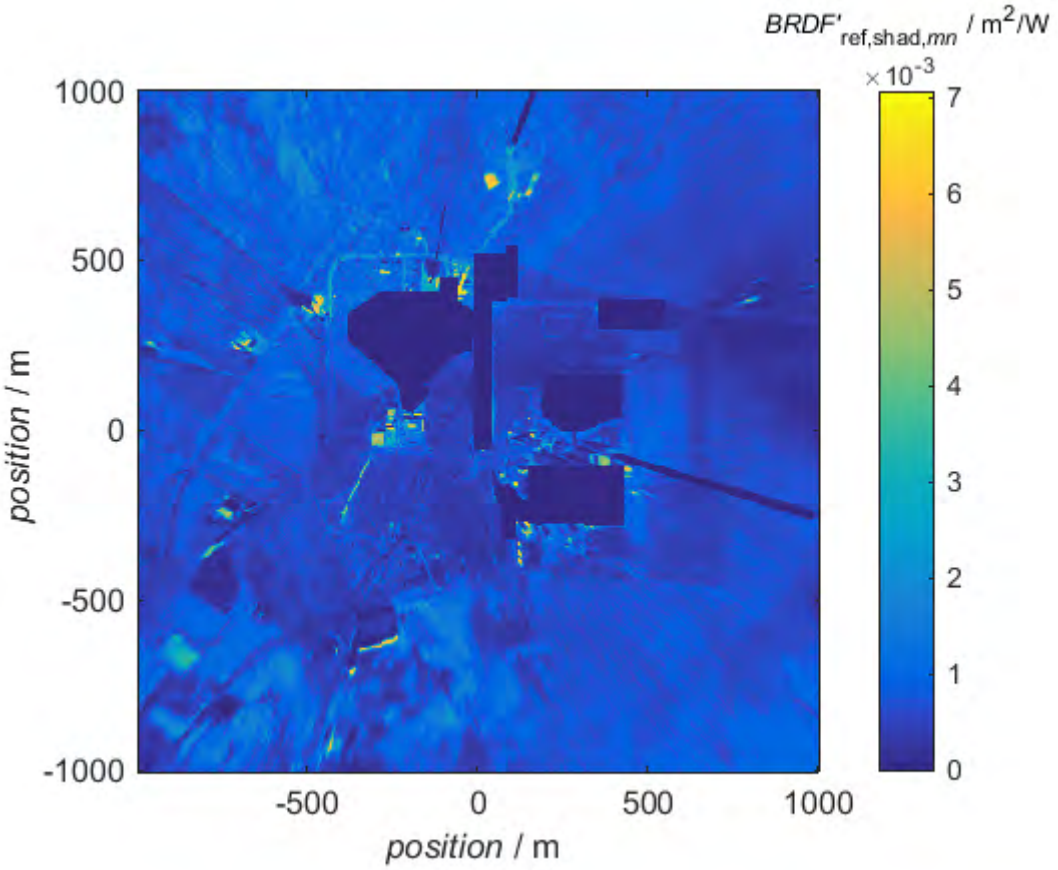

Figure 32: $BRDF'_{\text{ref,shad},mn}$ for the 19th of September 2015 at 12:57:00, UTC+01:00.

Ultimately, $BRDF'_{\text{sens},mn}$ is combined with $BRDF'_{\text{ref,shad},mn}$ to determine $f_{\text{map},mn}$ for each sensor. The sensors, their pixel difference values, the resulting $BRDF'_{mn}$ and $f_{\text{map},mn}$ are displayed in table 7.

The $f_{\text{map},mn}$ values are close one, so that the two methods for the determination of $BRDF'_{mn}$ seems reliable for the exemplary time stamp. The resulting $f_{\text{map,med}}$ is determined as unitless scale factor of 1.03.

Thus, every coordinate in the shaded area is determined by the application of equation 38.

5.5.4 Determining Remaining Areas for the Final Irradiance Map

The areas remaining are those, which are logically indexed 2 ("NaN") and 3 ("probably cloud"). Those areas are not going to be evaluated based on received data. Instead they are spartially interpolated bilinearly between the measured clear sky DNI (DNI_{sun}) and the shaded DNI ($DNI_{\text{shad},mn}$) with "griddata.m". Since the interpolation has weaknesses in the outer region of the area displayed, the remaining data is set to the mean irradiance

Sensor	$S'_{\text{diff,eval},mn}$	$BRDF'_{\text{sens},mn}$	$S'_{\text{diff,shad},mn}$	$BRDF'_{\text{ref,shad},mn}$	$f_{\text{map},mn}$
	/ pixel	/ $\frac{m^2}{kW}$	/ pixel	/ $\frac{m^2}{kW}$	/ -
NWN	0.651	0.786	0.670	0.763	1.03
NWW	0.480	0.744	0.494	0.563	1.32
NWC	0.361	0.435	0.371	0.423	1.03
NWS	0.327	0.395	0.338	0.385	1.03
SES	0.464	0.680	0.550	0.626	1.09
SWN	0.674	0.814	0.703	0.800	1.02
SWW	0.487	0.607	0.512	0.583	1.04
SWC	0.567	0.697	0.597	0.680	1.02
SWE	0.521	0.655	0.593	0.676	0.97
SWS	0.511	0.617	0.530	0.604	1.02
HP	0.459	0.588	0.492	0.560	1.05

Table 7: Shaded sensors and their pixel differences as well as their determined BRDF' values and each of the resulting $f_{\text{map},mn}$ for the 19th of September 2015, 12:57:00 UTC+01:00

value of the shaded area.

The GHI map is created afterwards, by using the relation between DNI, DHI and GHI, which is dependent on the SZA. For the entirety of the PSA the DHI is considered constant, as also applied in section 5.3. For this time stamp the DHI is measured as 244 watts per square meter and the SZA is 36°. It is determined by the Michalsky sun algorithm in [17]. The GHI for every coordinate is determined by the application of equation 8 to the existing DNI map.

The resulting DNI and GHImaps are displayed in figure 33, alongside with their segmentation result and the orthogonal image.

The irradiance map displays homogeneous borders and a clear isolation between the information of shadowless sensors and shaded sensors. Unfortunately, the interpolation method is creating distorted regions for the NaN values being interpolated. The map's values and their reliability is going to be discussed in section 6.3.

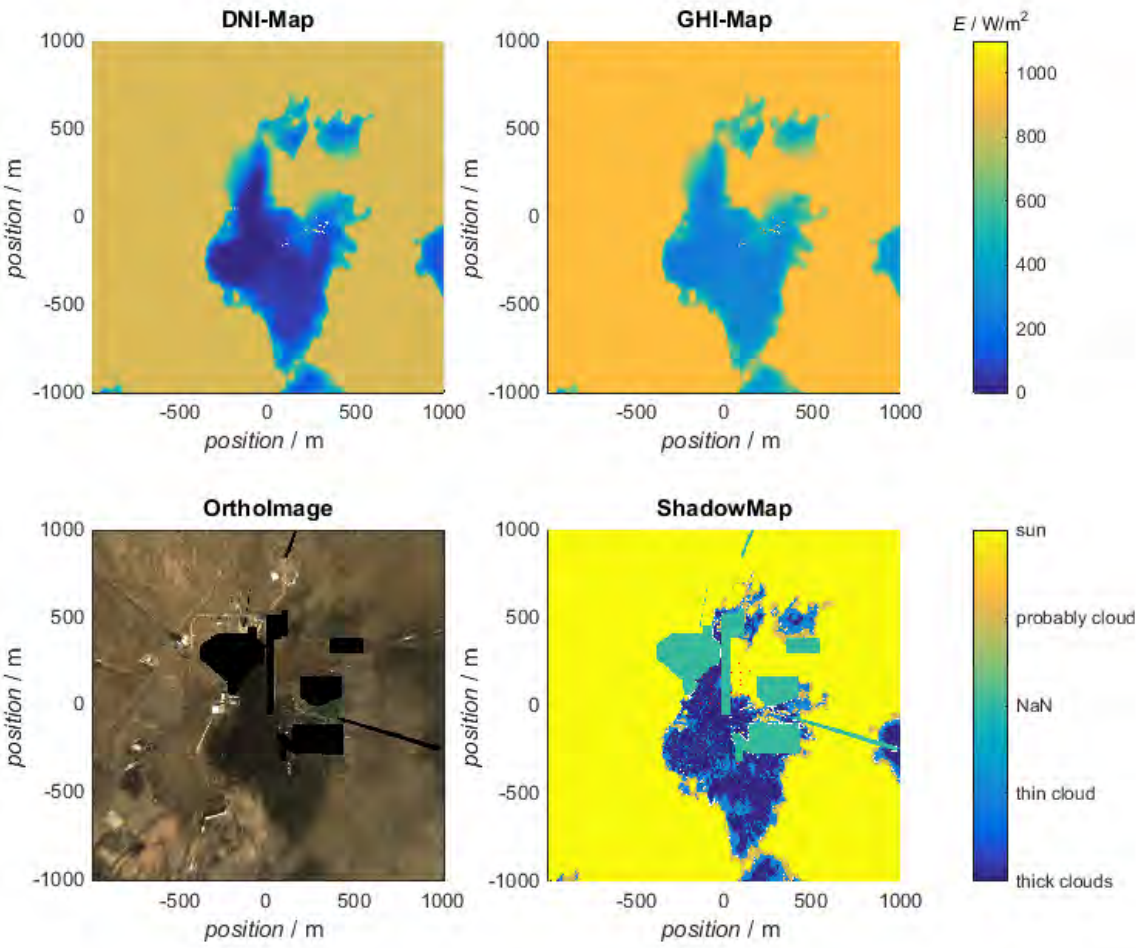

Figure 33: DNI map (top left) an GHI map (top right). The original orthogonal image (bottom left) and the segmentation (bottom right) are also displayed for the 19th of September at 12:57:00, UTC+01:00. The irradiance colorbar applies for DNI and GHI.

6 Evaluation of Results

To evaluate the generated irradiance data from section 5 and to give a statement about its accuracy, the process results are analyzed. Every program's step (merged orthogonal image, segmentation and created irradiance data) and its results have to be evaluated for that reason. Since the segmentation relies on the orthogonal images to be accurate to generate reliable results, the remaining distortion of the orthogonal images needs to be characterized. To analyze the segmentation exactly, the GPS features are compared with their position in the orthogonal image. To accomplish this, they will be determined manually in the orthogonal image. For the segmentation, the map factor $f_{\text{map,med}}$ will be evaluated for this. By doing so, a statement about the determination of the shadow's detection and position is gathered. To evaluate the calculated irradiance data, it will be compared with measured irradiance. For this, a grid sensor will be excluded. Afterwards, its generated values will be compared with the measured data. The accuracy of the generated data will display the evaluation of the system.

6.1 Assessment of the Merged Orthogonal Image

The main motivation of the camera calibration, which consists of the exact determination of its interior calibration parameters (x'_0,y'_0,c,$\Delta x'$,$\Delta y'$) and its exterior orientation parameters (X_0,Y_0,Z_0,ω,κ,φ), is to correctly project every pixel from the global system to the corresponding sensor coordinates. An orthogonal image, that contains no distorted areas, would be beneficial.

To determine this distortion, a chosen procedure reveals inaccuracies. While the orthogonal image is a map, that displays the assignment of each pixel to global coordinates, the in section 3.2.3 determined features can be applied to the orthogonal image. If every pixel is assigned exactly to the GPS coordinate it is supposed to describe, a perfect result has been obtained for these pixels.

Since there are 127 features to describe the observed area, systematical errors should be able do be identified. For the process however, only 119 features were able to evaluate, since the remaining eight are lying outside of the orthogonal image's area. The result of the distortion analysis is shown in figure 34.

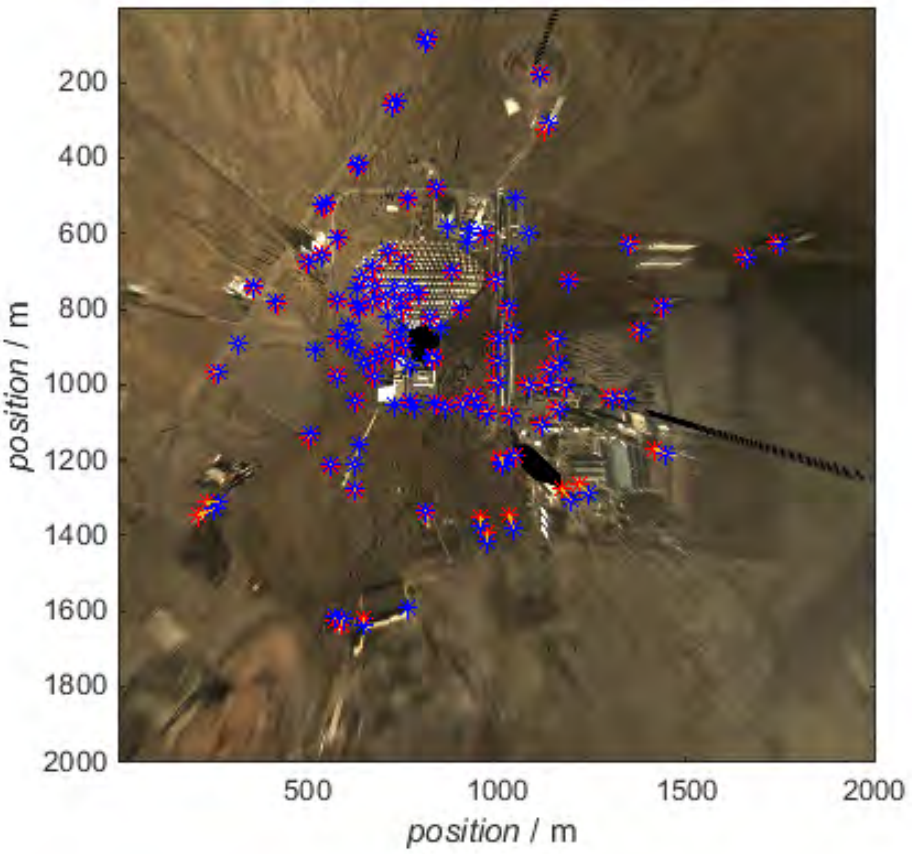

Figure 34: Result of distortion analysis. 119 GPS coordinate based features (red) and their residuals (orange) to the corresponding detected pixel (blue)

While looking at the indicated residuals, one area is significantly different from the others. The area which is covered by the east-south camera (direction also applies in this figure) displays much bigger residuals than the other image areas. While watching at the orthogonal image it also appears, that the area is not completely distorted. There are parts of the south-east camera's image, that don't fit to the border area of the south-west camera. The pixels in this area are distorted by up to 47 pixel. With the scale of 1 square meter per pixel the area is distorted by 47 meter. This value also represents the maximum value of the given residuals. The distortion can also be seen by taking a closer look at ways, fields, streets and other structures which are supposed to have straight borders or rectangular edges. Structures, that are straight, from a plain view perspective, should also appear straight in the orthogonal image. In contrast to the distorted area from the east-south camera, there is the area covered by the other cameras. The resulting mean value of the residuals is a total of 8 pixels, which leads to a mean distortion of 8 meters. This is only supposed to give a general impression about the accuracy, since it is

not representative for every pixel in the image. Another effect has been analyzed more specifically. The general distribution of all residuals is shown in figure 35.

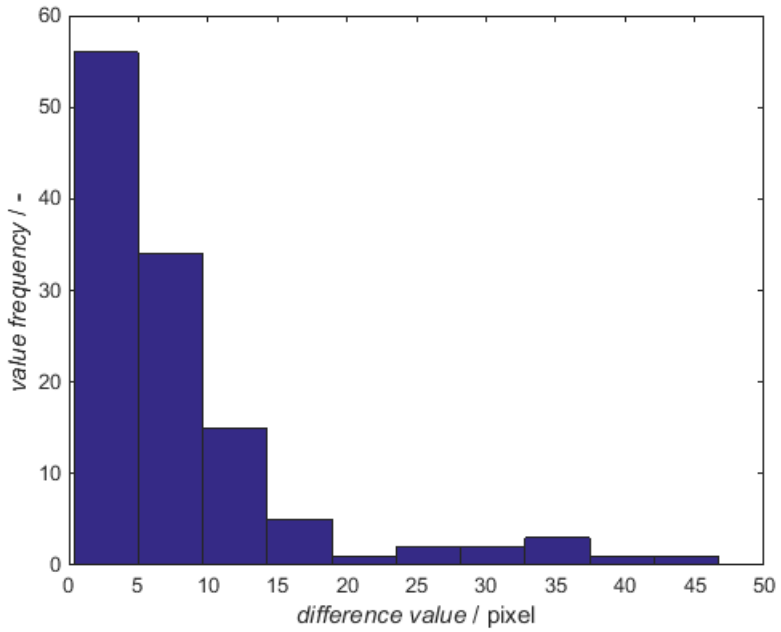

Figure 35: Distribution of residuals determined during the distortion analysis

The distribution also displays the residuals general appearance. While there is a dominating part of four cameras whose residuals are relatively small, the area covered by the east-south and the east-north camera are exhibiting relatively big deviations. The sensors used for the determination of irradiance maps are located in the area of these cameras. Therefore, there will appear segmentation errors caused by the distortion in this areas.

The distortion depends on the angle a camera is observing a coordinate on PSA with. This interacts with the fact that a ground model is the object, orthogonal images are projected onto. If the ground model differs from the area by a meter in height, the projected coordinate is also projected further back or forth. In an exemplary calculation a pixel in a distance of one kilometer was defined. Also, the camera's angle to this point at the end of the displayed image was calculated as 85.2° with height of the CESA-1 of 87 meters. The angle is defined between the CESA-1 tower and the camera's optical axis. Therefore, a scale factor for this distance to the shadow camera was defined. In a distance of one kilometer, a pixel deviation of 5 pixels already leads to a deviation of 57.5 meters.

Another factor is the ground model's height structure. If the ground model differs in a distance of a kilometer in height by one meter, this results in a deviation of 57.64 meters. Considering that there are differences in the height coordinate of the cameras as well as

the possible erroneous ground model, the distortion of the image with a tendency of rising distortion to the outer regions can be explained.

6.2 Assessment of Segmentation

For the evaluation of segmentation, an analysis of $f_{\text{map,med}}$ is performed. Recapitulating, $f_{\text{map,med}}$ is determined by dividing $BRDF'_{\text{sens},mn}$ by $BRDF'_{\text{ref,shad},mn}$, while $BRDF'_{mn}$ in general is determined by dividing a pixel difference by the corresponding DNI difference. If the sensors for the determination of $BRDF'_{\text{sens},mn}$ were segmented correctly, they would display a relation between pixel and DNI difference, which is close to the reference time stamps value. Therefore, f_{map} should be close to 1, if the segmentation was successful. This estimation is based on the linear relation between pixel and DNI difference. Consequently, it describes that the appearing pixel difference is connected to the DNI difference by $BRDF'_{mn}$. On the other hand, if the shadow was not segmented correctly, the appearing value will differ from the reference time stamp's value, since the determined pixel difference is not assigned to the correct DNI difference. Since the median of all single $f_{\text{map},mn}$ is determined, the evaluation will inform about those time stamps, when the segmentation failed entirely and not about the failed segmentation of a single sensor. Still, the incorrect determination of $f_{\text{map,med}}$ shall be evaluated, since this is causing erroneous irradiance maps.

For this purpose, the 19th September was evaluated. For the time span of 09:00-18:00, UTC +01:00, the program processed irradiance maps and by doing so, determined $f_{\text{map,med}}$. The factor's time stamp is also saved, to determine, whether there is a dependency of the system segmentation result on day time. The value for $f_{\text{map,med}}$ can only be determined, if sensors are actually shaded. For time stamps, when no sensor is shaded, $f_{\text{map,med}}$ is set to 1 by default.

186 time stamps remain when $f_{\text{map,med}}$ is determined with the mentioned methodology. Those calculated values and their frequency values are exemplary displayed in figure 36.

The display of this histogram was limited, since outliers distorted the display. The mentioned outliers were 8 values with the maximum value of 52.04. Others displayed values in the range of 20 - 30 while all of mentioned values displayed a value frequency of 1 - 2. Beside these outliers, it appears, that a tremendous percent of the calculated $f_{\text{map,med}}$ is close to 1 as expected. The statistic's outliers are caused by an erroneous calculation of $f_{\text{map,med}}$, which is caused a failed segmentation. These are caused by an erroneous sensor detection. It is assumed, that $BRDF'_{\text{ref,shad},mn}$ is mostly detected correctly, since it is calculated by the pixel difference between an image with complete overcast properties and the shadowless reference image as well as the clear sky DNI for this time stamp.

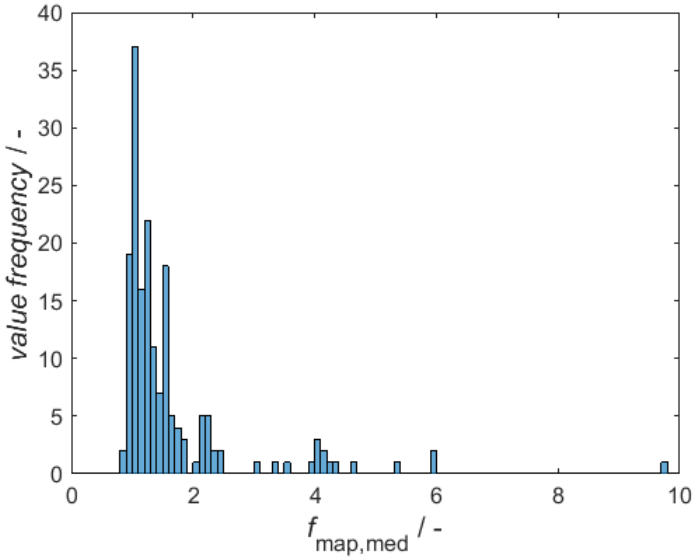

Figure 36: Value frequency of $f_{\text{map,med}}$ displayed over the calculated value for every evaluable time stamp

This procedure is automated properly and not considered to be potentially erroneous. The potentially more erroneous factor in this calculation is $f_{\text{map},mn}$. Recapitulating, it is determined by the DNI difference between clear sky DNI of the evaluated time stamp, respectively the appearing pixel difference for the evaluated time stamp (see equation 37). These parameters offer more conflict potential, since the shadow's detection respectively segmentation, needs to be accurate to classify the used sensors correctly. For time stamps, only one cloud's shadow passes by, the segmentation delivers reliable information as presented in section 5. It does display weaknesses during longer shading of the area, though. During time stamps, all sensors are shaded, it is difficult to determine the clear sky DNI. So far it is implemented by building the clear sky DNIs's median of the last 10 time stamps. This is potentially erroneous due to longer shaded time periods of the area. Therefore, the clear sky DNI is determined incorrectly and sometime displays values of 400 watts per square meter, although it should display values of 800 watts per square meter. A simple work around would be to use a clear sky model for such time stamps. Consequently, the appearing pixel difference remains constant while $BRDF'_{\text{sens},mn}$'s value rises. Still, $BRDF'_{\text{ref,shad},mn}$ remains constant, which causes the value of $f_{\text{map,med}}$ to rise as well and therefore they are significantly higher than expected. This is approved by the fact, that values for the clear sky DNI doesn't change that much within thirty seconds by experience. Also, the pixel differences should not differ that much as well, due to the defined time periods they are build from. Therefore, $f_{\text{map,med}}$ should generally display values close to one. While looking at the derived data, it also proves, that 64 percent of

the calculated values are in the range of 0.9-1.1. This range displays correct segmented time stamps. Due to longer shaded periods, there was a high degree of wrong detected sensor information.

Since it is assumed, that the entirely wrong calculated values are caused by a longer shaded periods for all sensors, $f_{\mathrm{map,med}}$ is plotted over the corresponding time stamp and visualized in figure 37

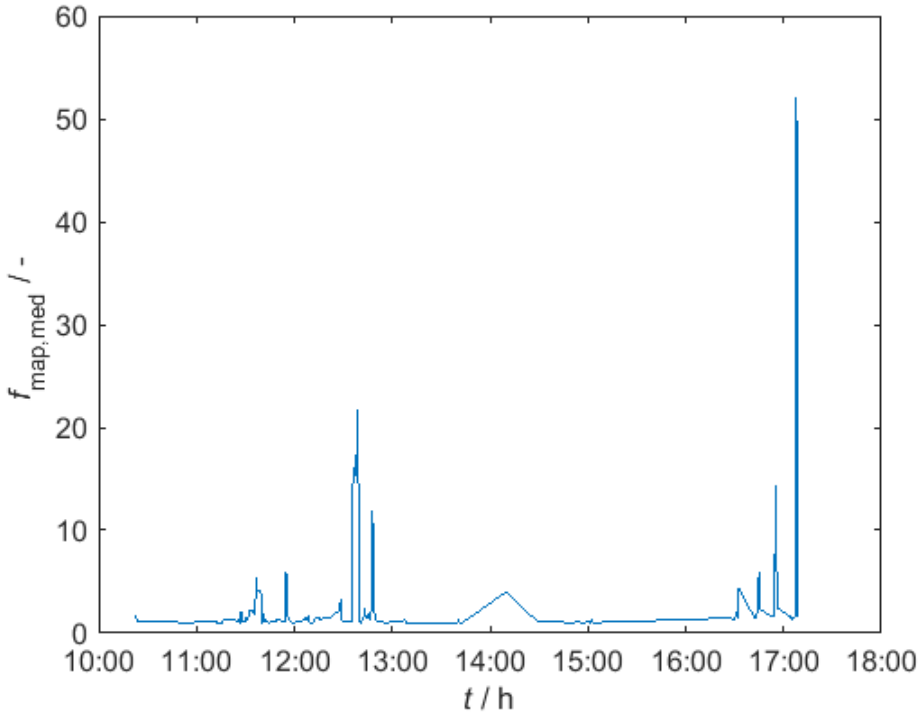

Figure 37: $f_{\mathrm{map,med}}$, displayed over time

The display of $f_{\mathrm{map,med}}$ over time also shows, that there is a dependency on the solar position. The segmentation fails during the time of 17:00-18:00 UTC +01:00 in the evening.

Also, there are effects, that affect the segmentation negatively. The pixel difference is build, relying on the reflection properties of the observed area. Hence, objects with a low degree of reflection, such as black bodies, are segmented worse than a plain field with dry grass. This also affects the sensor segmentation respectively their detection. The values in the momentary difference image differ by an absolute amount of 0.1, which is 25 percent of the considered maximum pixel value within a shaded area. This appears between two adjacent pixels, because of the reflection properties of the ground beneath. Here a more homogeneous display of a pixel difference would be beneficial.

6.3 Assessment of Irradiance Maps

To evaluate the generated irradiance maps, the generated information is compared with measured data. For this purpose one pyranometer is excluded, while the evaluation of an entire day is processed. Afterwards, the generated information is supposed to be close to the measured data. The difference between measured and generated information describes the discrepancy of the displayed model. Ideally, the generated data corresponds to the measured data. For the exclusion, the south-west grid's center sensor is chosen. This sensor was selected, since the south-west diamond is influenced less by reflecting effects from the environment. These effects are chosen to be excluded, so that the model's accuracy is displayed more accurately. The evaluated time period is also the 19th September 2015 from 09:00 to 18:00 UTC +01:00. The measured and the shadow camera derived data for the position of the south-west center sensor are displayed in figure 38.

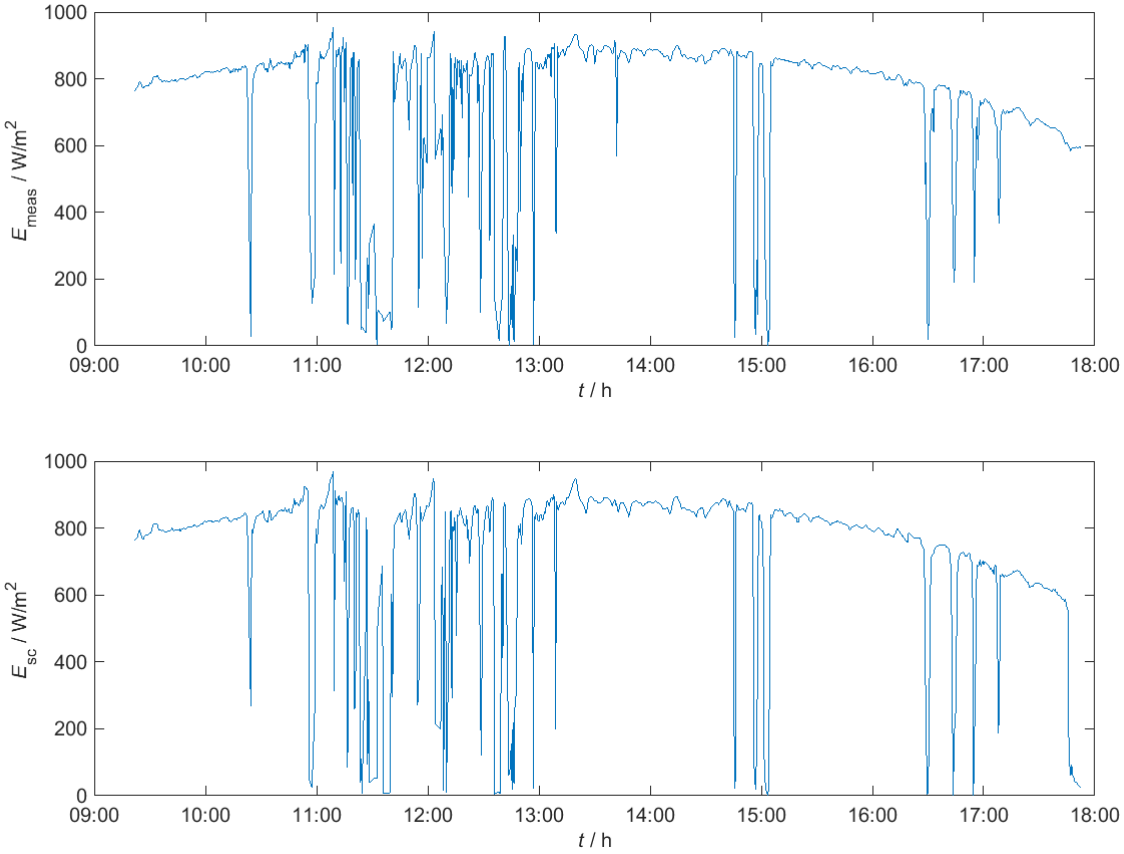

Figure 38: Measured irradiance by sensor information (top) compared to the generated DNI, using the introduced methodology (bottom) for the coordinates of the SWC pyranometer

Comparing both graphs, they seem pretty similar. A weakness of the system is visualized by these figures, though. The clear sky DNI does not display spikes towards high values

like the displayed DNI does. These spikes are caused by the determination of DNI through GHI with DHI from some distance away. Watching more closely, there are other errors. This is the case at in the end of the evaluated period, which was expected, regarding to the huge values for $f_{\text{map,med}}$ displayed in section 6.2. Also, there are huge differences from 11:00 to 13:00, UTC+01:00, when clouds passed the area. To get a better understanding of the system's accuracy, the corresponding difference between measured and generated data is displayed in figure 39.

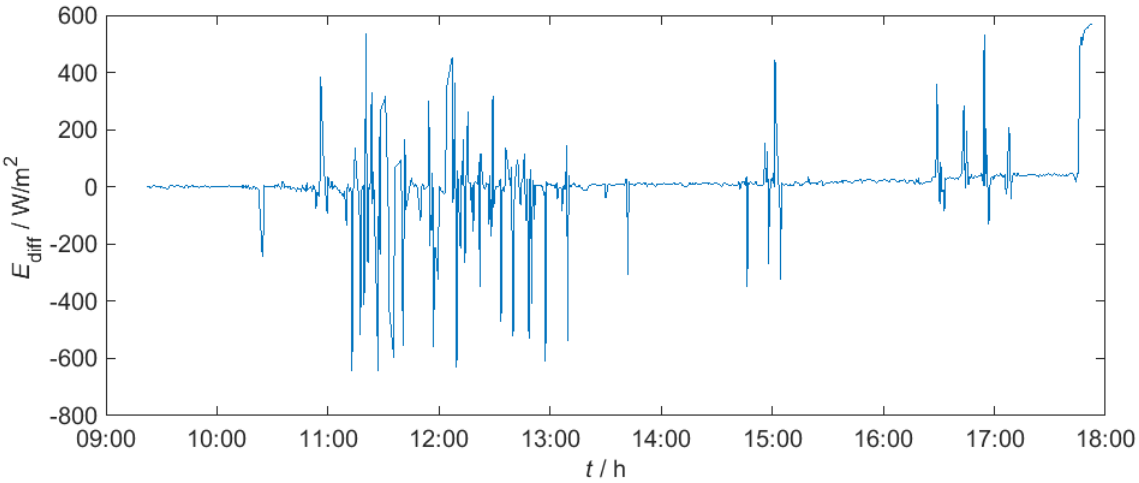

Figure 39: Difference values between measured and generated irradiance plotted over time.

The irradiance difference displayed shows weaknesses of the system. The system's main issue is the erroneous detection of the shadow's position, which is caused by the orthogonal image's distortion. It causes implausible values for $f_{\text{map},mn}$ and by doing so, it causes differences between measured and calculated DNI. If the shadow is detected at the wrong place, hypothetically twenty meters apart from its actual position, the shadow's pixel difference value doesn't apply for the observed sensor coordinate. The calculated DNI is therefore determined for another coordinate of the shadow. If a cloud respectively its shadow passes the sensor and covers it, according to the segmentation result, while in reality the sensor was located at the shadow's border with clear sky DNI, the appearing DNI difference displays values of up to ±600 watts per square meter. However, during well detected events, the difference between measured and generated events is considerably low and lies in the bounds of measurement uncertainty. The differences for well detected events displays values of mostly below 10 watts per square meter. The exemplary time stamp from section 5 corresponds this values. The sensor's value and the segmented pixel difference are detected correctly. This is confirmed by the evaluation of time stamps with a $f_{\text{map},mn}$ close to one. For the evaluated time stamp in section 5, the difference between calculated and measured irradiance is only 7 watts per square meter. Finally,

differentiation has to be made. There are differences, for situations, the shadow's edge is passing the measurement device. Meanwhile, the shadow is segmented correctly for other sensors, since they were shaded. Hence, this effect appears in different sensors, while the cloud's shadow is passing by and therefore the irradiance map is distorted by the same distance as the shadow.

7 Summary

A shadow camera based system for the creation of irradiance maps was developed in this thesis. The existing shadow camera system was enhanced by the implementation of ground based irradiance measurements from radiometers. By processing the camera's raw images and using them in combination with the irradiance measurements, DNI- and GHI-maps for the area of PSA were created.

The existing shadow camera system was expanded by four cameras. These enable a 360° evaluation of shaded areas for PSA. Besides, all cameras were calibrated respectively re-calibrated to determine their orientation parameters. With these parameters, orthogonal images for an area of four square kilometers were created. Besides, the created orthogonal images were cleaned from effects, that affect the exact determination of shadows. Moreover, erroneous effects for the segmentation, like specular reflecting objects, were excluded. Previously established binary maps were expanded to quinary maps, that contain more detailed information about the shaded areas. Furthermore, the entire shadow is now able to detected, since the application of one threshold was not sufficient. A method to determine DNI differences from pixel differences was established to combine DNI measurements with shadow camera data. It requires an entirely shaded time stamp, that serves as a reference for the area being ideally not influenced by DNI. This method also enables the determination of DNI differences for areas, using the shadow camera's information. For this, the $BRDF'_{mn}$ was determined from parts of shadow camera images. This allowed to determine DNI in areas, that are only known by their pixel difference. Radiometers are used, to define the relation, since the DNI differences for a completely shaded and a sunny reference time stamp are required.

The result's evaluation shows, that there still is a distortion in the orthogonal image. As seen in section 6.2, the distortion reaches its maximum values in the area, covered by east-north and especially the east-south camera. The appearing distortion values for this area reached 47 pixels for the given data points in a 1 square meter per pixel resolution. The detection of shadows works generally and only considering the sensors, that are detected as shaded. For those sensors, that are sorted out by the median procedure, the differences are displaying values of up to 600 watts per square meter. As described in section 6.3, this is caused by wrong detected shaded areas. These effects are mainly appearing in the shadow's edge area. Also, an erroneous detection of the clear sky DNI leads to huge differences, since it is used for the sunny area. This leads to differences to sensors, that displayed clear sky DNI. In general, the model generated values within $\pm$ 15 watts per square meter to ground measurements, for time stamps the cloud's shadow was detected correctly.

To improve wrong determined $f_{\text{map},mn}$ values, they should be observed. All of them should be displayed and the the outliers analyzed, to approve the erroneous determination of $f_{\text{map},mn}$ in shadow edge areas. To solve this problem a correction to the shadow's position would be beneficial. Regarding the fact, that the orientation was created in the same way for all six cameras, the camera's calibration isn't the only issue for the deviation in the orthogonal image. The ground model might also be a cause for this distortion, since there is a general tendency on rising distortion towards the south. It is assumed, that the ground elevation in the south of PSA is not characterized correctly in the code. Considering this and the uncertainties, that are implied to the calibration of these cameras and the fact, that the pyrheliometer values are used to calibrate other radiometers, the irradiance information should be valued higher. Therefore, a correction to the shadow's position, depending on the appearing irradiance values, is a possibility to solve this problem. This would also solve the problem of wrong detected clear sky DNI. This could improve the evaluation of shaded areas in further work.

List of Abbreviations

BRDF bidirectional reflectance distribution function
CC cloud coverage
CCD charge coupled device
CMOS complementary metal oxide semiconductor
CPV concentrating photovoltaics
CSP concentrating solar power
CTAER Centro Tecnológico Avanzado de Energías Renovables
DHI diffuse horizontal irradiance
DISS direct solar steam
DLR Deutsches Zentrum für Luft- und Raumfahrt
DNI direct normal irradiance
GHI global horizontal irradiance
GPS global positioning system
HTF heat transfer fluid
HP high precision
m.a.m.s.l. meters above mean sea level
NaN not a number
PSA Plataforma Solar de Almería
RGB Red Green Blue
SSPS Small Solar Power Systems
sRGB standard Red Green Blue
SZA solar zenith angle
TSI total solar irradiance
UTC universal time coordinated
WSI whole sky imager

List of Figures

List of Tables

Bibliography

[1] Boyle, Godfrey: Renewable Energy. Ed. by Boyle, Godfrey. 2nd ed. Oxford University Press, Oxford in association with The Open University, Milton Keynes. 2004.

[2] Coimbras, Carlos F.M.: "Concentrated Operational Forecast Systems for GHI and DNI Solar Ramps". In: *COST ES 1002 WIRE international workshop on sky cameras*. 2014.

[3] Demant, Christian, Streicher-Abel, Bernd, and Springhoff, Axel: Industrielle Bildverarbeitung - Wie optische Qualitätskontrolle wirklich funktioniert. Springer Verlag. 2002.

[4] GLOBAL POSITIONING SYSTEM STANDARD POSITIONING SERVICE PERFORMANCE STANDARD. Department of Defense. 4th Edition. 2008.

[5] Gross, Vitalij: System zur Erfassung der zeitabhängigen Verschattung von Standorten potenzieller Solarfelder. Bachelorarbeit, Hochschule für Technik und Wirtschaft, Berlin. 2010.

[6] Gueymard, Christian A.: "Solar Radiation, Introduction". In: *Solar Energy* 86.12 (2012), pp. 9705–9744.

[7] Guide to Meteorological Instruments and Methods of Observation. World Meteorological Organization. 2008.

[8] Günther, Matthias: Advanced CSP Teaching Materials. Tech. rep. Deutsches Zentrum für Luft- und Raumfahrt e.V., 2011.

[9] Hecht, Eugene: Optik. 4. Auflage. München: Oldenbourg Verlag. 2004.

[10] IEC/4WD 61966-2-1: Colour Measurement and Management in Multimedia Systems and Equipment - Part 2-1: Default RGB Colour Space - sRGB. INTERNATIONAL ELECTROTECHNICAL COMMISSION, May 1998.

[11] Kleissl, Jan: Solar Energy Forecasting and Resource Assessment. Ed. by Kleissl, Jan. Elsevier, Academic Press. 2013.

[12] Liou, Kuo-Nan: An Introduction to Atmospheric Radiation. Ed. by Dmowska, Renata, Holton, James, and Rossby, Thomas. 2nd ed. Vol. 84. International Geophysics Series. Elsevier, Academic Press. 2002.

[13] Litwiller, Dave: "CMOS vs. CCD: Maturing Technologies,Maturing Markets". In: *PHOTONICS SPECTRA* (2005).

[14] Luhmann, Thomas: Nahbereichsphotogrammetrie: Grundlagen, Methoden und Anwendungen. Herbert Wichmann Verlag - Heidelberg. 2000.

[15] M24M Kamerahandbuch. 3rd ed. Mobotix AG. D-67722 Langmeil, 2013.

[16] Meister, Gerhard: "Messung der spektralen Reflexionsfunktion (BRDF) ausgewählter Oberflächen bei natürlicher Beleuchtung". MA thesis. Universität Hamburg, 1995.

[17] Michalsky, Joseph: “The astronomical almanac’s algorithm for approximate solar position”. In: *Solar Energy* 40.3 (1988), pp. 227–235.

[18] Müller, Sebastian: “Entwicklung und Validierung eines wolkenkamerabasierten Systems zur Echtzeiterstellung solarer Einstrahlungskarten”. Masterthesis. Hochschule Nordhausen, 2015.

[19] Nettlau, Janina: “Entwicklung und Erprobung eines Messsystems zur kontinuierlichen Strahlungsmessung an Strahlungsempfänger solarer Turmkraftwerke”. MA thesis. Universität Stuttgart, 2008.

[20] Oberländer, Daniel, Prahl, Christoph, Wilbert, Stefan, Müller, Sebastian, Stanicki, Badrudin, and Hanrieder, Natalie: “Cloud shadow maps from whole sky imagers and voxel carving”. In: *International Conference Energy & Meteorology*. 2015.

[21] Poynton, Charles: Digital Video and HDTV Algorithms and Interfaces. Morgan Kaufmann Publishers. 2003.

[22] PVPerformance - Modeling Collaborative. English. U.S.Department of Energy. 2014. URL: `https://pvpmc.sandia.gov/modeling-steps/1-weather-design-inputs/sun-position/`.

[23] Scaramuzza, Davide: Omnidirectional Camera and Calibration Toolbox for Matlab. Eidgenössische Technische Hochschule Zürich. Rämistrasse 101, 8092 Zürich, Schweiz.

[24] Scaramuzza, Davide, Martinelli, Agostino, and Siegwart, Roland: “A Toolbox for Easily Calibrating Omnidirectional Cameras”. In: (2006).

[25] Schwarzbözl, Peter, Gross, Vitalij, Quaschning, Volker, and Ahlbrink, Nils: “A LOW-COST DYNAMIC SHADOW DETECTION SYSTEM FOR SITE EVALUATION”. In: *In SolarPACES conference*. 2011.

[26] Solar energy - Specification and classification of instruments for measuring hemispherical solar and direct solar radiation. International Organization for Standardization. 1990.

[27] THEME ENERGY.2013.2.9.2 - Methods for the estimation of the Direct Normal Irradiation (DNI). 2013.

[28] Wilbert, Stefan: “Determination of Circumsolar Radiation and its Effect on Concentrating Solar Power”. PhD thesis. Rheinisch-Westfälische Technische Hochschule Aachen, 2014.

[29] Wilbert, Stefan: “Weiterentwicklung eines optischen Messsystems zur Bestimmung der Formabweichungen von Konzentratoren solarthermischer Kraftwerke unter dynamischem Windeinfluss”. Diplomarbeit. Rheinische Friedrich-Willhelms-Universität Bonn, 2009.

[30] Wilbert, Stefan, Nouri, Bijan, Jessen, Wilko, Schwandt, Marko, Meyer, Richard, and Kraas, Birk: Best Practices for Solar Irradiance Measurements with Rotating Shadowband Irradiometers. Solar Resource Assessment and Forecasting 46. Solar Heating & Cooling Programme - International Energy Agency, 2015.

Appendix

A Shadow Camera Images

A.1 Raw Images

Figure 40: Raw images from shadow cam east-north (left) and shadow cam east-south (right)

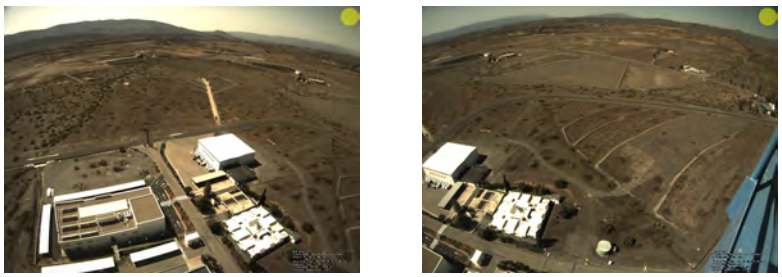

Figure 41: Raw images from shadow cam south-east (left) and shadow cam south-west (right)

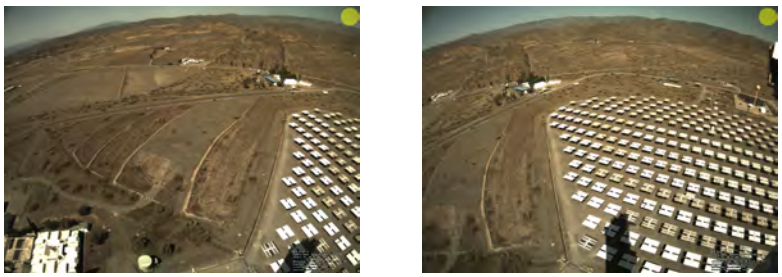

Figure 42: Raw images from shadow cam west-south (left) and shadow cam west-north (right)

A.2 Camera Position

Figure 43: Camera's position, installed on CESA-1. 1 EN = east-north, 2 ES = east-south, 3 SE = south-east, 4 SW = south-west, 5 WS = west-south, 6 WN = west-north

B Interior Calibration Pattern

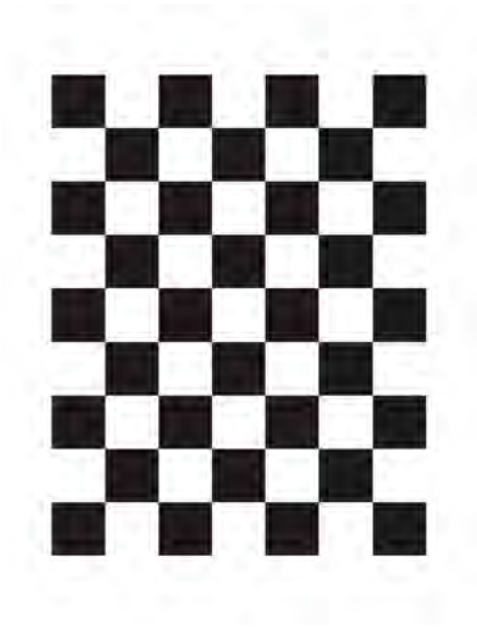

Figure 44: Calibration pattern to determine inner orientation parameters